The Characterization and Calibration
of the
OSIRIS Infrared Imager

A Thesis

Submitted to the Faculty of Graduate Studies and Research

in Partial Fulfillment of the Requirements

for the Degree of

Master of Science

in the Department of Physics and Engineering Physics

by

Adam Edward Bourassa

Saskatoon, Saskatchewan

i

To Ed and Joan Bourassa, my parents.

Abstract

OSIRIS, a Canadian built instrument on-board the Swedish-led remote sensing satellite, Odin, consists in part of three single lens imagers that measure near infrared light from atmospheric scattering and emission. A full calibration of the imaging system is required to remove all instrument dependent effects that modify the observations.

This work presents the characterization and calibration of the OSIRIS imaging system in an attempt to produce observations that are instrument independent measurements of the atmospheric brightness. The required product is the number of photons per second emitted, or scattered, from the atmosphere that are within the sampling wavelength range and incident on the detector area in the instrument field of view.

A major portion of the present work involves understanding the dark current production mechanisms and the development of a technique to characterize the dark current and manufacturer imposed electronic offsets. It is demonstrated that with a current set of dark calibration images, the developed algorithm effectively removes the dark current and electronic offsets over a wide operating temperature range. The relative calibration of pixels is presented in terms of the electronic gain, or flat field response, and the angular look direction. It is apparent that a change in the relative pixel gain occurred between pre-flight calibration and the first in-flight images. However, it is shown that with a recalculation of the flat field response using in-flight images, an acceptable gain calibration is obtained. The angular look direction of the pixels is determined from the results of two separate in-flight experiments. The characterization and removal of the stray light signal is shown to be effective.

Finally, the absolute calibration of the instrument is presented. While several issues remain to be addressed, the comparison with a simple atmospheric brightness model provides a first order verification of the results.

Acknowledgements

Contents

List of Figures

Glossary of Terms

α A calibration constant relating the observational units to the physical units of brightness.

A/D   Analog to digital conversion.

brightness   The incident optical power coming from a unit area in a wavelength interval in a particular direction. Preferred units for this thesis are photons/s/cm^2/nm/sterad.

CTIA   The Capacitive Trans-Impedance Amplifier circuit configuration used for the imager photodiodes.

DCP Dark Calibration Parameters.

DN Digital Number. The units of the raw imager data product.

f Dimensionless normalized filter shape.

FOV   Field of view.

image   A single exposure of the linear array detector containing an observation from each of the 128 pixels.

InGaAs   Indium Gallium Arsenide; the composition of the OSIRIS imager photodiodes.

IRIS   InfraRed Imaging System; specifically the three linear array imagers of the OSIRIS instrument.

k	Pixel index.
limb	The line of sight where the curvature of the Earth meets the blackness of space. In this context, it will taken as a line of sight column of atmosphere through which light is measured at a given tangent height.
LS	Lambertian source, i.e. a source with uniform brightness occupying the entire field of view.
MAS	Minimum atmospheric signal altitude, i.e. the lowest tangent altitude containing no atmospheric signal.
n	Image index.
NDI	Normalized detector irradiance.
O	Imager signal specifically due to electronic offset of an image, i, or a pixel, k.
Odin	A Swedish led remote sensing satellite launched on February 20, 2001.
OSIRIS	Optical Spectrograph and InfraRed Imaging System. A Canadian built remote sensing instrument on board the satellite Odin.
pixel	A single imaging element in the linear array detector composed of an InGaAs photodiode and a corresponding amplification circuit.
profile	The vertical distribution of an atmospheric parameter.
r	Reference pixel index.
S	Electrical signal read-out from the imager in units of DN.
t	Exposure time.
T	Temperature.

Chapter 1

Introduction

1.1 OSIRIS and the Atmospheric Airglow

The study of the scattering and emission of light by atoms and molecules in the atmosphere, referred to as the airglow, provides understanding of important physical processes. As satellite technology becomes more reliable and less cost prohibitive, remote sensing of the airglow from a satellite platform is becoming a feasible opportunity. The scientific yield from a satellite mission has vast potential; high resolution global coverage is achievable in relatively short time with monitoring continuing over the period of years. Previously studied and notable airglow emissions, which are the focus of the OSIRIS imager mission, are the $(a^1\Delta_g \rightarrow X^3\Sigma_g^-)$ infrared atmospheric system of molecular oxygen and the OH Meinel vibrational-rotational band airglow.

1.2 The OSIRIS Imager

OSIRIS, <u>O</u>ptical <u>S</u>pectrograph and <u>I</u>nfra<u>R</u>ed <u>I</u>maging <u>S</u>ystem, is a Canadian instrument onboard the Swedish-led remote sensing satellite, Odin. OSIRIS, as the acronym suggests, is a combined UV-visible spectrograph and a near infrared imaging system (IRIS). The IRIS consists of three single lens imagers, each measuring a

different wavelength region with a linear array of InGaAs photodiodes. The imager measures light, emitted and scattered from molecules in the atmosphere, at wavelengths that are relevant to ozone and some other species that play an important role in the chemistry and dynamics of the stratosphere and mesosphere.

The IRIS, like any real photodetection system, must be calibrated in order to remove instrument dependent effects from the measurement and to convert the electronic output of the system to the units of physical brightness. This calibration work is the focus of the thesis.

The stages of the characterization and calibration can be divided into two broad categories due to the nature of the instrument: effects of the photodetection system and effects of the optical system. As an introduction to the thesis work, a summary of the issues involved with practical photodetectors and a simple optical system is presented followed by a summary of the stages necessary in the calibration of the OSIRIS imager.

1.3   Photodetection Systems

A photodetector is a radiation sensor; it is a device that measures the intensity of a light signal. Most often the measurement is made through a conversion of the incident light into an electrical signal.

The most basic type of photodetector is a thermal detector. These devices use a material in which the temperature varies with the incident optical power. Thermal detectors have a very limited sensitivity and often respond very slowly to changes in incident radiation.

Ideally, a photodetector would be sufficiently sensitive so that the result of the measurement would simply be a count of the number of incident photons. Realistic detectors that approach this type of sensitivity are based on one of two main principles: the "external" photoelectric effect or "internal" electron excitation.

For practical materials, the efficiency of external photoelectric effect devices is

greatly reduced for wavelengths above 700 nm due to the characteristic work function of the material. For wavelengths greater than those in the visible range, and for visible light detection as well, internal electron excitation devices made of semiconductor material can be used for photodetection. Semiconductor detectors are of two main classes: the photoconductor and the photodiode. A photoconductor is a semiconductor that has a resistance that changes with varying illumination, whereas a photodiode is a semiconductor diode that generates a current that is a function of the illumination of the detector. Photodiodes are generally the detector of choice in modern day applications, including the OSIRIS imaging array, because they are small and have high speed response and good sensitivity.

1.4   Calibration of a Photodetector

An ideal photodiode produces a current that is directly proportional to the number of incident photons within the optical passband. A real photodiode, however, generates a current that is not only proportional to the radiation power, but is also a function of the temperature of the device. Consideration must also be given to the wavelength response of the detector. A photodiode has a quantum efficiency that is a characteristic of the material properties and describes the efficiency of conversion of a photon to output current. The quantum efficiency is a function of the wavelength of the incident photon; lower energy photons, still within the passband of the measurement may be more or less efficiently converted to output current than higher energy photons.

In general, the full calibration of a photodiode detection system involves the removal of all instrument dependent effects from a measurement of a radiation source. Generally, the calibration of a photo-detection system involves two stages:

- Dark current removal,

- Absolute calibration.

The dark current removal refers to the correction for the output current that is generated due to the temperature of the device that (hopefully) does not depend on the incident radiation of the measured source. The absolute calibration is the conversion of the measured output current of the photodiode to a physical brightness of the radiation source. This must take into account the wavelength and temperature dependencies of the quantum efficiency of the photodiode and effects due to the read-out electronics that measure the photo-generated current. The result of the calibration is an instrument independent measurement of the brightness of the source.

1.5 Calibration of an Optical System

Optical systems for scientific measurement range from single lens systems to complex interferometers and spectrometers with various calibration issues related to their specific function. In general, however, the characterization of even the simplest optical system involves measurement of the angular field of view and the corresponding axis of the line of sight relative to the instrument frame. Optical effects that can affect the measurement of the incident signal include diffraction and scattering of out-of-field light from external surfaces into the field of view. These effects depend on the physical properties of the optical system, the viewing geometry and the illuminating source.

1.6 Calibration of the OSIRIS Imager

The OSIRIS imager is a photodetection instrument that contains both electrical and optical components that can affect the measurement of the incident signal. The main stages in the calibration of the imager are:

- Dark current removal,

- Relative gain calibration,

- Relative look direction registration,

- Stray light removal,

- Absolute calibration.

The dark current removal and the absolute calibration are very important aspects of the instrument calibration. Added to these are stages that result from the optical system and multi-detector feature of the imager. The relative gain calibration attempts to correct for variations in the gain and quantum efficiency of each individual photo-diode, or pixel. The relative look direction registration is a determination of the field of view and central line of sight of each pixel. The stray light removal is a correction for effects of the optical system; these include baffle scatter and diffraction. A good understanding and effective characterization of each of these terms results in a calibration that yields an instrument independent measure of the source brightness.

1.7 Outline

A background of the OSIRIS mission that includes an instrument description and a survey of past measurements relevant to the atmospheric molecular emission that are the focus of the imager observations are given in Chapter 2.

Chapter 3 details the dark current characterization in terms of modern semi-conductor physics and presents a technique developed especially for the removal of dark current terms in a multi-detector system. Chapter 4 presents the relative calibration, including the gain and the look direction, of the detectors in the imager. There is an emphasis on understanding the gain of the system in flight.

The stray light correction is presented in Chapter 5. Previous modelling of the out of field scatter is summarized and a technique is detailed that allows for the removal of the stray light by using in-flight measurements for characterization. Chapter 6 contains a summary of the current work on the absolute calibration and includes a comparison of flight data with a simple atmospheric model of scattered sunlight. Finally, a summary of the results of the calibration together with recommendations for future work is given in Chapter 7.

Chapter 2

Background: The OSIRIS Imager

2.1 Introduction

This chapter provides a background of physical properties of the molecular emissions measured by the OSIRIS imager and a history of the discovery and previous measurements of the emissions. It also provides a description of the imager instrument and the satellite orbit and viewing geometry. Background details specific to each stage in the calibration are included in the following chapters as each issue is addressed.

2.2 The Oxygen InfraRed Atmospheric Band

The first observation of the excited state of molecular oxygen $O_2(a^1\Delta_g)$, commonly referred to as 'singlet delta', was made by Herzberg (1934) from detection of strong atmospheric absorption of the solar spectrum at 1.27 μm. This transition is the (0,0) band, referring to the vibrational states of the electronically excited singlet delta state and ground state molecule, $O_2(X^3\Sigma_g^-)$, respectively.

Vallance Jones and Harrison (1958) unsuccessfully attempted to measure twilight emission of the $(a^1\Delta_g \rightarrow X^3\Sigma_g^-)$ transition from the ground because of strong

atmospheric absorption at low altitudes. They were, however, able to measure an emission at 1.58 μm in the evening twilight from a transition of $O_2(a^1\Delta_g)$ to the first vibrational level of the ground state state molecule: the (0,1) band. This detection was observed as an enhancement of the already documented spectral emission of the Meinel system of OH. The observation of the emission in the evening twilight and the failure to observe the emission in the morning confirmed the long lifetime of the $a^1\Delta_g$ state. Vallance Jones and Harrison believed that the emission was due to a resonant-phosphorescent process with sunlight. In further study of the (0,1) band, Vallance Jones and Gattinger (1963) report a strong seasonal variation in the brightness of the 1.58 μm emission which is not satisfactorily explained by the resonant-phosphorescent theory. They proposed the creation of the $O_2(a^1\Delta_g)$ state through photo-dissociation of ozone, O_3, as shown in Equation 2.1. Confirmation of the ozone dissociation hypothesis was made in 1966 through observations of the emission brightness during solar eclipse (Gattinger and Vallance Jones, 1966).

$$O_3 + h\nu \rightarrow O_2(a^1\Delta_g) + O. \tag{2.1}$$

The first successful observation of the (0,0) transition at 1.27 μm was made in 1962 from high altitude aircraft at 13 km (Noxon and Vallance Jones, 1962). A series of balloon flights by Evans et $al.$ (1967) measuring the 1.27 μm emission from 30 km further confirmed the ozone dissociation hypothesis.

A height profile of the midday 1.27 μm emission was obtained in 1968 with rocket-borne instrumentation (Evans et $al.$, 1968). The profile was in excellent agreement with the theoretically obtained profile that assumed production of singlet delta through ozone photo-dissociation. However, a second distinct layer of emission, in excess of the prediction, was observed in the upper mesosphere. Similar height profiles were obtained with later rocket experiments (Haslett et $al.$, 1969; Wood, 1972). Further study of the diurnal variation in the brightness of the singlet delta lead to the discovery of additional production mechanisms including a proposed dissociation of vibrationally excited OH producing $O_2(^1\Delta_g)$ in the nighttime

(Llewellyn and Solheim, 1978).

In the 1980's, satellite technology was becoming globally popular as a means to study the atmosphere. The Solar Mesospheric Explorer, SME, was launched in 1981 with the objective of studying ozone in the stratosphere and mesosphere. One of the main instruments on board was a spectrometer that measured a band centered at 1.27 μm (Barth *et al.*, 1983). SME data supplied confirmation of the excess emission in the mesosphere reported by Evans *et al.* (1968), and provided evidence that supported the source of the emission as a secondary ozone peak (Thomas *et al.*, 1983). Variation in the mesospheric ozone concentration was also measured in the 1980's during a total solar eclipse (Bantle *et al.*, 1983).

As the ability to measure the singlet delta emission increased, the need for a greater understanding of the production and loss mechanisms became important. Because the $a^1\Delta_g$ state has a relatively long radiative lifetime, the interpretation of observations is especially difficult during non-steady state periods such as twilight. Complex models of the time dependent photo-chemistry were developed in order to properly interpret the measurements (López-González, 1989; Mlynczak and Olander, 1995). An accepted model of the production chain for airglow at 1.27 μm that includes interactions with ozone and molecular oxygen was developed by Mlynczak *et al.* (1993).

Closely tied to the Infrared Atmospheric Band of oxygen is the vibrationally excited Meinel hydroxyl (OH*) emission. Similarities in the nightglow height profile between the $O_2(a^1\Delta_g)$ emission and OH* emission measured by Evans *et al.* (1973) show that both excited states may be created by a reaction between atomic oxygen and HO_2 (Wood, 1972). Llewellyn and Solheim (1978) suggested that a reaction between atomic oxygen and OH* creates singlet delta and atomic hydrogen.

The dominant reaction in the creation of OH* is a reaction between ozone and atomic hydrogen, as shown in Equation 2.2.

$$O_3 + H \rightarrow OH^* + O_2. \tag{2.2}$$

Thus, the simultaneous measurement of ozone, through the $O_2(a^1\Delta_g)$ emission, and the direct measurement of OH*, through the Meinel emission, can be used to infer the atomic hydrogen profile.

Measurement of both $O_2(a^1\Delta_g)$ and OH* emissions is still continued as they provide important information on the energy budget of the mesosphere. The mesosphere is a dynamic area of the atmosphere and little is known about the causes and effects of energy deposition. The simultaneous measurement of mesospheric ozone, molecular oxygen, hydrogen, and hydroxyl with high temporal and spatial resolution can provide important information that will help in our understanding of this area of the atmosphere.

2.3   The OSIRIS Instrument

OSIRIS, on the Odin satellite, is a combined optical spectrograph and infrared imaging system (Murtagh *et al.*, 2002). The IRIS, InfraRed Imaging System, is itself composed of three separate co-aligned single lens imagers. Figure 2.1 is a schematic of the entire OSIRIS instrument with the imager optical assembly clearly visible on the left side.

The imagers have parallel bore-sights; each one consists of an identical baffling system with a 23 mm diameter aperture, a ZnSe plano-convex lens, a narrow-band interference filter, and a one-dimensional linear array of 128 thermo-electrically cooled InGaAs photodetectors placed in the focal plane of the lens. A schematic of the lens-detector system is shown in the simple conceptual drawing in Figure 2.2. Approximately 20 photodectors at the end of each array are covered with a mask in order to provide a continuous measure of the dark signal in the array. These masked pixels are critical for dark current removal. There is a shutter between the lenses and the detectors for the collection of dark images. There are also two small infrared sources in the region between the lenses and the detectors intended for calibration purposes.
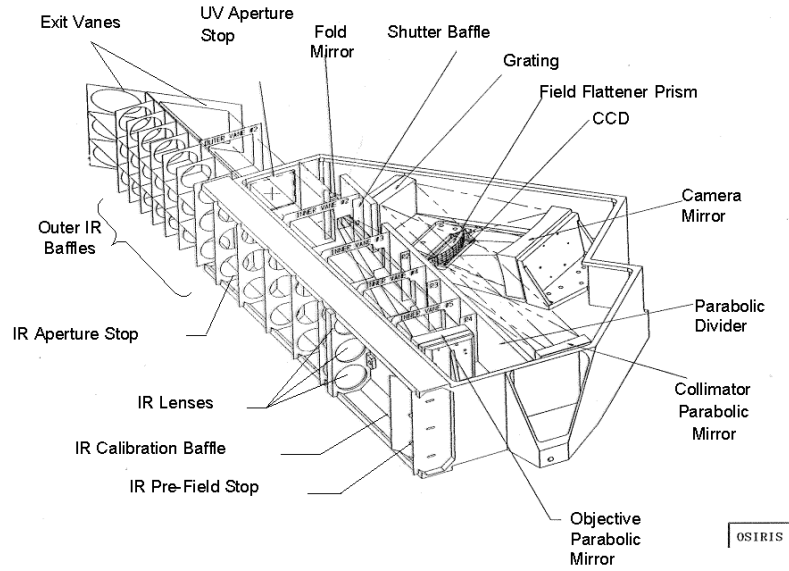
Figure 2.1: A schematic of the OSIRIS instrument.
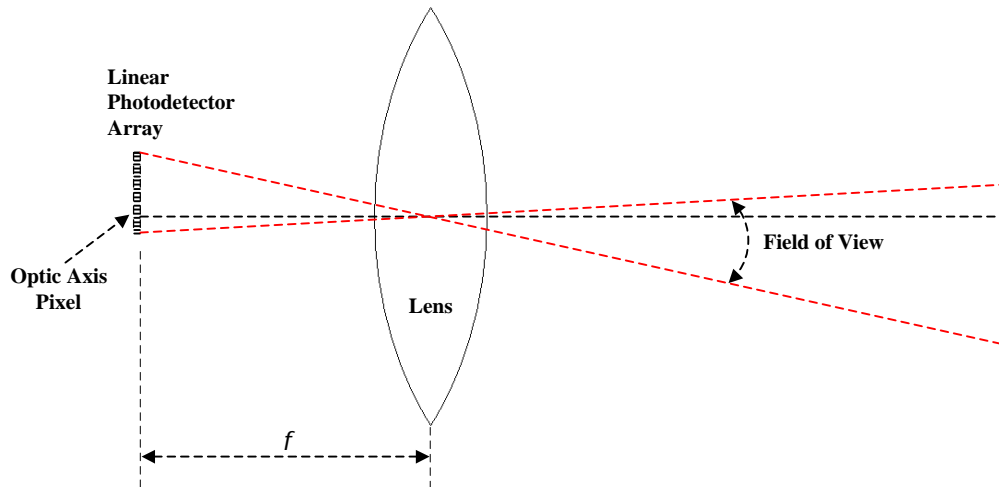
Figure 2.2: Conceptual schematic of a single lens linear array imager.

2.4 Satellite Platform Viewing Geometry

The Odin satellite carries both OSIRIS and a sub-millimetre radiometer, or SMR, this latter is used for both aeronomy and astronomy as the satellite has a dual mission: astronomy and aeronomy. The requirements of both missions impacted the orbit selection and the operating modes of the satellite. Odin is currently in a sun-synchronous dusk-dawn orbit with an inclination of 97° and at an altitude of approximately 600 km; this provides both maximum solar power and thermal protection. The inclined orbit, together with 18h00 local time ascending node, means that each orbit tracks through both sunrise and sunset, except for two periods per year when the orbit track follows the terminator.

In this orbit, each photodetector, or pixel, in the linear array of the imager has a field of view of 1 km in the vertical by 2 km in the horizontal when mapped on to the Earth's limb. Therefore, each imager, or channel, which contains approximately 110 pixels that measure light, makes simultaneous measurements of 110 km of the vertical atmospheric limb profile.

In astronomy mode, OSIRIS is switched off. In aeronomy mode, the optical axis of the instrument has a field of view through the atmosphere at a certain tangent height. For aeronomy, the satellite is in either "nod" mode or "stare mode". In stare mode, the tangent height of the optic axis is fixed such that all pixels have a different tangent height. In nod mode, the entire satellite oscillates over 2 degrees every 4 minutes such that the optic axis scans through approximately 100 km in the limb. Figure 2.3 is a conceptual drawing of the sun-synchronous orbit showing the different science modes and the solar condition. A sketch of the limb scattering and emission geometry is also shown. Another picture of the earth, the orbit and the atmosphere is shown to scale in Figure 2.4. The satellite track is shown in black and the atmosphere in blue. The first 100 km of the atmosphere is represented by the thickness of the blue line. The 2 degree field of view of the imager is shown for several locations of the satellite, represented as red dots.
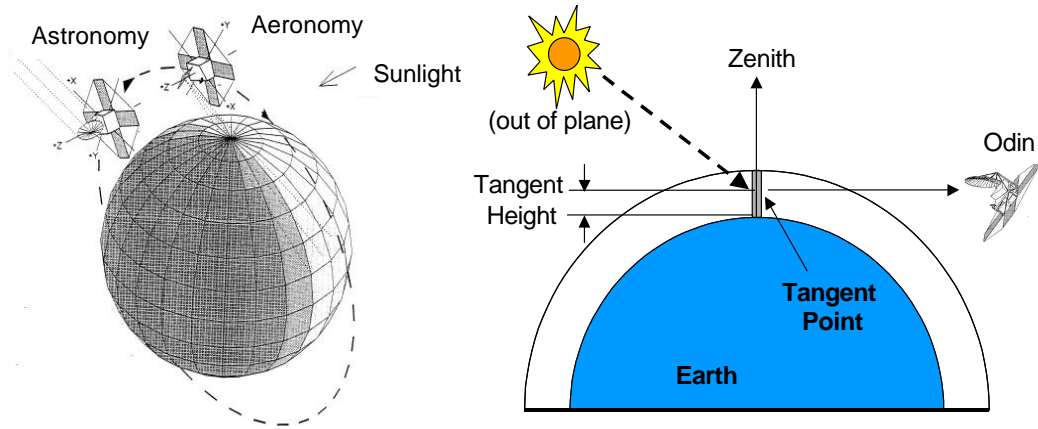
Figure 2.3: (a) Conceptual sketch of the orbit showing the science modes of the satellite. (b) Remote sensing limb scatter and emission geometry.
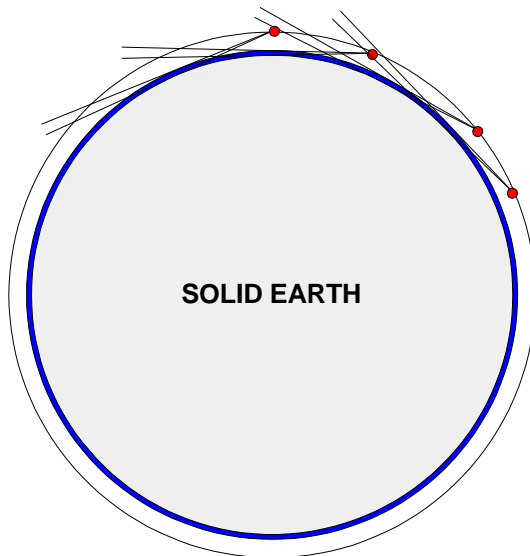
Figure 2.4: Odin orbit geometry shown to scale.

2.5 The Airglow and IRIS Filters

Each of the imager channels has an interference filter in the optical path and directly attached to the photodetector array. Channels 2 and 3 primarily measure airglow emission from the oxygen Infrared Atmospheric band at 1.27 μm with 10 nm wide filters centered at 1.273 μm and 1.263 μm, respectively. Figure 2.5 shows a plot of the calculated emission band spectrum of the $O_2(a^1\Delta_g \rightarrow X^3\Sigma_g^-)$ transition overlayed on the normalized filter shape for channel 3. In a similar fashion, the filter of channel 1, 40 nm wide, is centered at 1.530 μm, and measures the OH Meinel vibrational-rotational 4-2 and 3-1 band airglow after sunset and scattered sunlight during the daytime.
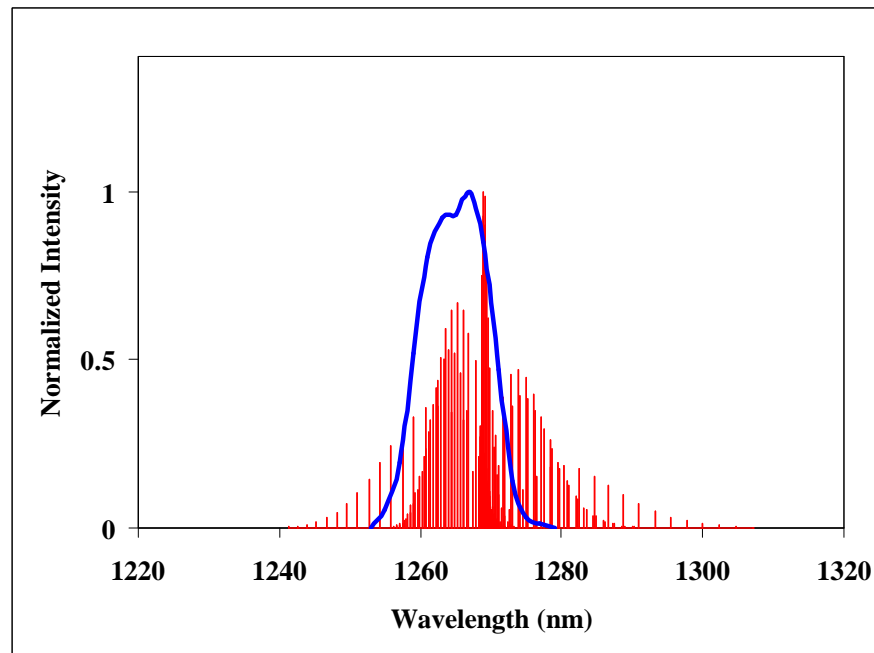
Figure 2.5: Synthetic $O_2(a^1\Delta_g)$ emission band spectrum and the measured channel 3 average filter shape.

2.6 Calibration Data

Before the launch of the satellite, the flight model of the OSIRIS instrument was used to make a number of calibration measurements at different facilities. As well, ongoing calibration measurements are being made at regular intervals in flight.

There were three main pre-flight calibration data sessions, each with a different primary objective. The calibration data taken in Calgary, Canada, were extensive. Many dark images were taken over a large wide of exposure times and temperatures. In addition, a scanning monochromator was used to measure the wavelength response and the relative gain response. In Linköping, Sweden, a less extensive set of dark current measurements was made. The optical alignment and measurement of the field of view were performed in Toulouse, France.

Ongoing in-flight calibration measurements include dark current monitoring using the imager shutter system to take dark images, and an attempt to monitor any changes in the system gain by imaging the small calibration sources inside the baffle and shutter system.

2.7 IR Imager Mission Summary

The primary objective of the IRIS portion of the OSIRIS instrument is the high resolution measurement of the stratospheric and mesospheric emissions related to the photolysis of ozone. The Oxygen InfraRed Atmospheric Band and the closely related Meinel Hydroxyl Bands are simultaneously measured in a line of sight brightness integral over 100 vertical kilometers at the tangent point with a resolution of approximately 1 km. The data will be used to derive concentrations of species, including ozone and hydrogen, on a global basis. The primary capability of the imaging technique is that the observations can be used as inputs to a tomographic inversion that can provide information on variations in horizontal structure with unprecedented resolution (Degenstein *et al.*, 2003). Together, the height profile of

species concentrations and information about horizontal structure in high resolution provide new insight into the dynamics and energy budget of the mesosphere.

Chapter 3

Dark Current and Electronic Offset

3.1   Introduction

In this chapter, the characterization of the dark current and the electronic offsets of the detector array are presented. Each pixel in the array has a unique dark current characteristic and an independent electronic offset relative to the other pixels. There is also an image electronic offset, which varies randomly from image to image, that is dependent on the readout electronics imposed by the manufacturer. Because of this image dependent offset, a difference technique is used that allows the relative offset of the pixels and the dark current to be characterized, as functions of temperature and exposure time, so that the dark current can be removed from those images that contain atmospheric signals.

3.2   Dark Current in a Linear Detector Array

Each photodiode in the InGaAs linear detector array produces a current that is thermally generated. This signal is present even when there is no incident optical

signal and is, therefore, called dark current. Because each pixel in the array has slightly different operating characteristics due to imperfections in the manufacturing process, the dark current of each pixel must be considered independently. For the OSIRIS imager, with 3 channels each with 128 pixels, there are essentially 384 different detectors that must be individually considered. The common algorithm for the calibration of instruments that generate dark current, such as CCD's and imagers, is to record and store a dark image that is subtracted from subsequent images that contain optical signal. Several complications must be considered in the case of this imager because of the random image electronic offset, and the range of exposure times and operating temperatures.

3.2.1 Light Detection and Shot Noise

A photodiode detects light through the generation of a free electron-hole pair, an electron in the conduction band and a hole in the valence band, by the absorption of photons with energy that is greater than the bandgap energy of the material. If the electron-hole pair is created within the depletion region of the diode, the charges drift in a direction based on the electric field in the junction that is set up by the diffusion of the majority carriers. The drifting charge generates a reverse current that is proportional to the number of incident photons called the photocurrent, I_{ph}, as shown in Figure 3.1. The magnitude of the photocurrent depends on the drift velocities of the charges in the material as they travel through the junction. It is also a function of the number of electron-hole pairs generated, which depends on both the quantum efficiency of the photon absorption process and the number of incident photons. Since the field in the junction is not uniform over the junction width and because the photons are absorbed over a distance in the material that depends on the photon energy, or wavelength, modelling the exact time dependence of the photocurrent on the optical power is not trivial.

The sensitivity of a photodetector is determined by the magnitude of the random
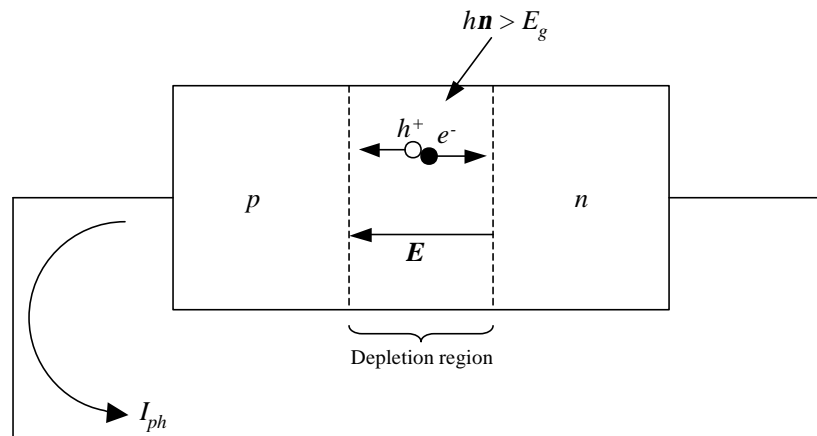
Figure 3.1: Generation of reverse photocurrent through photon absorption.

fluctuations in the photogenerated current. Any signal level must be greater than the random fluctuations in order for it to be distinguished from the noise. Since photons are discrete, the absorption of the photons and the creation of the charge that generates the photocurrent is a discrete process. This means that even for a constant incident optical power, the random nature of the discrete charge arrival causes current fluctuations about the average value. These random fluctuations, governed by the Poisson probability distribution, are known as "shot noise".

In a photodetector, electron-hole pairs are created through the photon absorption process; however, a temperature dependent dark current is also generated. Since this is also a discrete process the dark current, which has a "dc" value at a given temperature, exhibits these random fluctuations so that there is shot noise associated with dark current. Figure 3.2, based on Figure 5.19 from Kasap, 2001, is a simple plot of typical dark and illuminated photocurrents over time. They were generated for normally distributed values that vary about an average value for each type of current. It should be noted that the random fluctuations about the illuminated
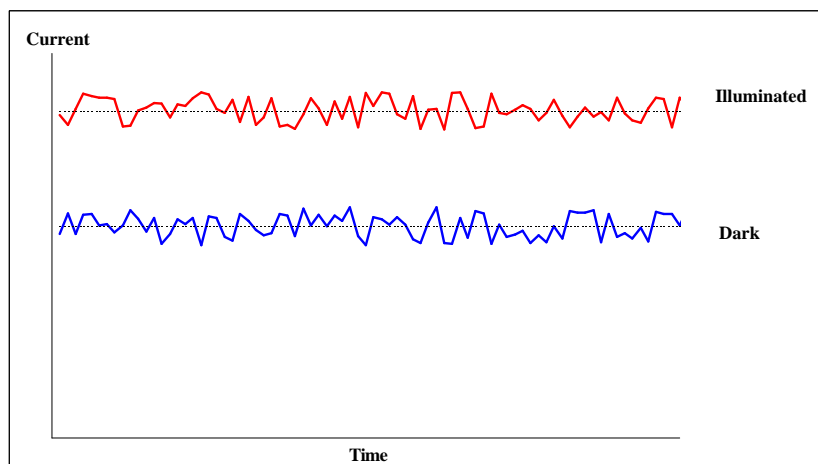
Figure 3.2: Theoretically generated plots of shot noise in typical dark and illuminated currents.

current dc value, which represents a sum of the dark current and the photocurrent, do not necessarily correspond to the fluctuations about the dark current dc value.

3.2.2 The Capacitive Trans-Impedance Amplifier

Each pixel in the linear InGaAs array is composed of a photodiode in a sample-and-hold Capacitive Trans-Impedance Amplifier (CTIA) configuration as shown by the schematic in Figure 3.3. In the CTIA configuration, the p-type anode of the photodiode, which shares a common n-type substrate with the other photodiodes in the array, is connected to the inverting input of a differential operational amplifier. The feedback loop consists of an integrating capacitor in parallel with a reset transistor. When the photogenerated charge from the photodiode causes a slight change in voltage at the inverting input of the op-amp, the output of the op-amp, which has an open loop gain of several orders of magnitude, drops significantly. This voltage drop is connected to the inverting input through the feedback capacitor and causes the photogenerated charge to flow on to the feedback capacitor to oppose the original voltage change at the input.

20
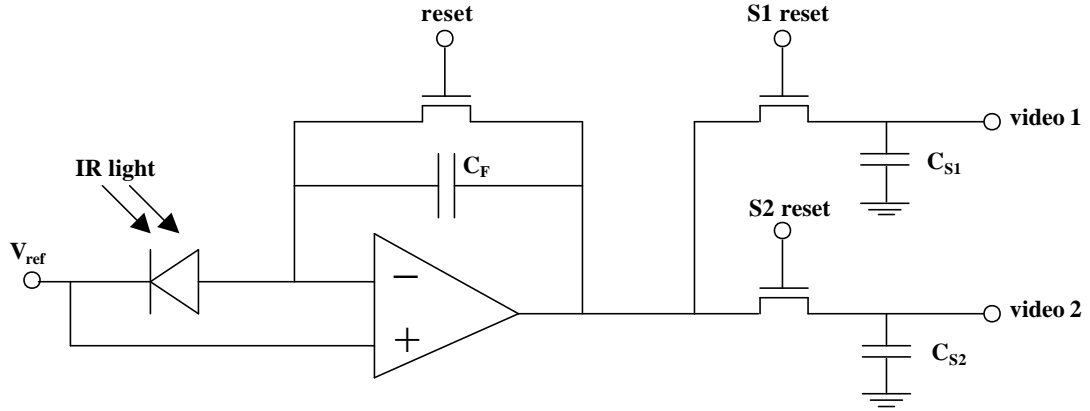
Figure 3.3: The CTIA Photodiode Configuration.

The two sample and hold capacitors are used to sample the voltage of the integrating capacitor at the start and end of the integration time by pulsing the reset transistors. These start-time and end-time voltages are input to a second differential op-amp that amplifies the voltage difference that is proportional to the charge collected from the photodiode during the integration time. This voltage difference is input to a 14 bit A/D converter, read-out, and stored in memory.

3.2.3   Non-Ideal Zero Bias Operation of the Photodiode

In an ideal CTIA configuration, both of the inputs of the op-amp are held at the same reference voltage such that the photodiode is not biased. Under zero-bias conditions, the diffusion of majority carriers across the depletion region is balanced by the carriers drifting in the opposite direction due to the internal electric field in the junction set up by the exposed ions from the diffusion process. In the absence of incident radiation, electron-hole pairs can be thermally generated by energetic

21

vibrations of the crystal bonds promoting electrons from the valence band to the conduction band (and holes from the conduction band to the valence band). When an electron in the conduction band encounters a hole in the valence band, it falls from the conduction band to occupy the lower electronic energy state of the hole, the process is called recombination. The excess energy in the transition is lost as an emitted photon or as heat in a lattice vibration. In steady state, under no applied bias, the rate of thermal generation is equal to the rate of recombination. Therefore, in the dark where there is no generation of photocurrent, the net current, at any temperature, from the photodiode is zero.

For individual photodiodes, adjustments of the CTIA are available to create the zero bias condition and ensure a minimum dark current. However, with linear photodiode arrays, these adjustments are not possible and the voltage bias of each pixel has a small magnitude that varies randomly and depends on the precision of the photolithography construction. The result is that each diode in the array can be operating under zero-bias, forward-bias, or reverse-bias conditions.

3.2.4 Forward Bias Operating Condition

Under a forward bias, as shown in Figure 3.4, the potential, V_0, of the photodiode junction (Figure 3.1) is lowered by the voltage of the external source of voltage V to $(V_0 - V)$. This decrease in the potential increases the probability that a hole in the p-side will overcome the potential barrier and diffuse to the n-side. The same is true for electrons that diffuse across the junction from the n-side. This diffusion results in an excess of minority carriers in the neutral sides of the diode. Injected electrons in the neutral p-region recombine with the many holes in this region, these holes can be replenished by the positive terminal of the battery, connected to the p-side under forward bias. The supply of injected electrons, diffusing to the p-side from the n-side, can be maintained by the negative terminal of the battery connected to the n-side. The result of the forward bias of the battery is a maintainable forward

current due to the diffusion of minority carriers that is described by the well-known Shockley equation,

$$J_{\text{diff}} = C_1 n_i^2 \left[\exp\left(\frac{eV}{k_B T} \right) - 1 \right],$$ (3.1)

where V is the applied voltage, T is the temperature, k_B is the Boltzman constant, and C_1 is a constant that depends on the material properties such as the hole and electron diffusion lengths, and the donor and acceptor concentrations. The intrinsic concentration, n_i, in the semiconductor is given by,

$$n_i = \sqrt{N_c N_v} \exp\left(-\frac{E_g}{2k_B T} \right),$$ (3.2)

where E_g is the bandgap, the energy difference between the conduction band and the valence band, and N_c and N_v are the effective densities of states at the conduction and valence band edges, respectively, and represent the number of available electronic states, or wavefunctions, at the corresponding band energy. These densities, Equation 3.3, which depend on the effective carrier mass, m_e^* for electrons and m_h^* for holes, are comparatively weak functions of temperature.

$$N_c = 2 \left[\frac{2\pi m_e^* k_B T}{h^2} \right]^{\frac{3}{2}}; \quad N_v = 2 \left[\frac{2\pi m_h^* k_B T}{h^2} \right]^{\frac{3}{2}}.$$ (3.3)

During the minority carrier diffusion, there is some recombination of electron-hole pairs in the depletion region as well as in the neutral sides. This also results in a sustainable external forward current, described in Equation 3.4, called the recombination current,

$$J_{\text{recom}} = C_2 n_i \left[\exp\left(\frac{eV}{2k_B T} \right) - 1 \right],$$ (3.4)

where C_2 is a constant that depends on the width of the depletion region and on the mean recombination time of the electrons and holes.

The total forward current, defined in the traditional direction of allowed current flow through an ideal diode, and in this case generated in the dark, is a sum of the diffusion current and the recombination current, or

$$J_{\text{dark}} = J_{\text{forward}} = J_{\text{diff}} + J_{\text{recom}}.$$ (3.5)

It is important to note that J_{diff} is proportional to n_i^2 whereas J_{recom} is proportional to n_i which means that the temperature dependence of each term is different, this is shown in Equations 3.6 and 3.7,

$$J_{\text{diff}} \propto \exp\left(-\frac{E_g}{k_B T}\right), \tag{3.6}$$

$$J_{\text{recom}} \propto \exp\left(-\frac{E_g}{2k_B T}\right). \tag{3.7}$$

Under forward bias, the photocurrent is still a reverse current, so the forward current due to diffusion and recombination, J_{forward}, subtracts from the photocurrent, as shown in Figure 3.4, such that the total measured current, J_{total} is

$$J_{\text{total}} = J_{\text{ph}} - J_{\text{dark}} = J_{\text{ph}} - J_{\text{diff}} - J_{\text{recom}}. \tag{3.8}$$

3.2.5 Reverse Bias Operating Condition

When a photodiode is in a reverse bias operating condition, as shown in Figure 3.5, the voltage drop from the external source is mainly across the resistive junction of the diode. The junction potential is raised by the external source, voltage V, from V_0 to (V_0+V). The forward current diffusion can no longer be maintained since the battery cannot supply holes to the injected electrons in the p-side because of the reverse bias. However, a small reverse diffusion current flows due to the concentration gradient in the minority carriers from the edge of the depletion region, where the concentration is zero, to the neutral bulk where the the concentration is small but non-zero. For example, electrons diffuse from the bulk p-side to the edge of the depletion region where they are accelerated by the electric field and drift toward the n-side. This is a sustainable current since when the electron reaches the n-side, it can recombine with a hole supplied by the positive terminal of the battery. This reverse diffusion is called the reverse saturation current and is also described by the Shockley equation, Equation 3.1, with a negative bias voltage, $V = -V_r$, such that

$$J_{\text{diff}} = C_1 n_i^2 \left[\exp\left(\frac{-eV_r}{k_B T}\right) - 1\right]. \tag{3.9}$$

24

It should be noted that when the reverse bias voltage is greater than the thermal voltage, $k_B T/e = 25$ mV, J_{diff} no longer depends on the magnitude of the bias voltage but is "saturated" at $-C_1 n_i^2$.

Electron-hole pairs that are thermally generated in the depletion region also contribute to the reverse current since the internal electric field will separate the charge and drift them toward the neutral regions. Electrons, which drift toward the n-side, can recombine with a hole supplied by the positive terminal of the battery. This reverse thermally generated current is given by

$$J_{\text{gen}} = C_3 n_i, \tag{3.10}$$

where C_3 is a constant that depends on the width of the depletion region and on the mean thermal generation time of the electron-hole pairs. Since the width of the depletion region depends on the magnitude of the reverse bias, increasing the bias also increases J_{gen}.

Again, it is important to note that the two terms that contribute to the dark reverse current depend differently on n_i and, therefore, have different temperature dependence similar to that in Equations 3.6 and 3.7. Thus, under a reverse bias configuration, the total current under illuminated conditions is a reverse current that is the sum of the photocurrent and the dark current, which is composed of the diffusion current and the thermally generated current,

$$J_{\text{total}} = J_{\text{ph}} + J_{\text{dark}} = J_{\text{ph}} + J_{\text{diff}} + J_{\text{gen}}. \tag{3.11}$$
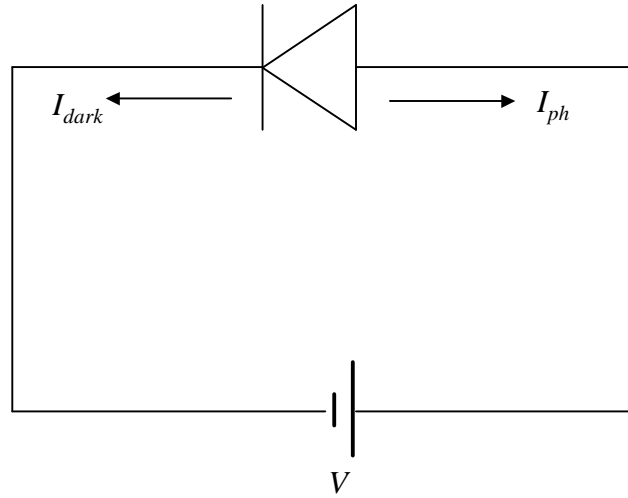
Figure 3.4: A forward biased photodiode.
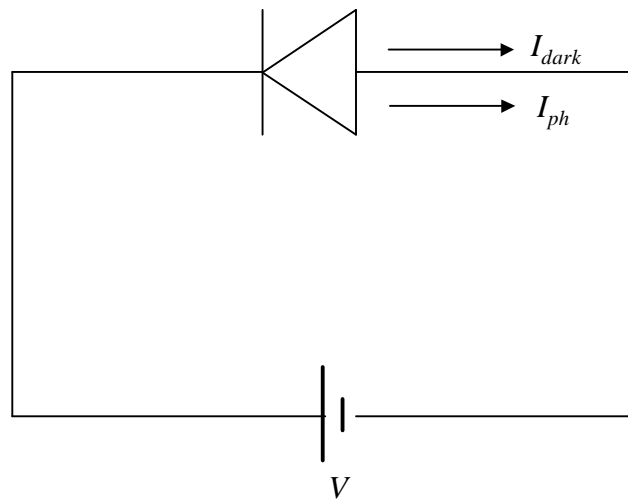
Figure 3.5: A reverse biased photodiode.

3.3   D.C. Offset of a Linear Detector Array

The signal measured by each pixel in an image is essentially a measure of the voltage difference sampled at the start and end of each exposure. However, because of the random bias of each diode due to the non-ideal CTIA circuit, shown in Figure 3.3, the dark current may be subtractive causing the voltage difference between the start and end of the exposure from an image with greater dark current than photocurrent to be negative. For this reason, a uniform D.C. offset voltage is electronically applied to the entire detector array at the start of each integration. This image offset is imposed by the manufacturer of the hardware and cannot be externally controlled by user software. Also, each pixel begins the integration with an unique offset, relative to the other pixels, that is small compared to the magnitude of the image offset.

3.3.1   Image Offset and Relative Pixel Offset

Unfortunately, the uniform D.C. offset voltage applied to each image is not constant from image to image. However, the relative bias that is unique to each pixel remains constant. Therefore, a dark, cold, short exposure image, which contains a negligible amount of dark current because of the low temperature and short exposure time, consistently has the same shape due to the constant pixel bias, but has an average value that varies randomly with the image offset. Figure 3.6 is a plot of a typical dark, cold image from the OSIRIS imager channel 3. Note that the image is centered near 2500 DN (Digital Number) which is about 15% of saturation of the 14-bit (zero-based 16383 DN full well) A/D converter. The independent axis in this case is the vertical axis showing pixel number. This convention is used here, and following, as it follows the typical atmospheric science convention to plot height on the vertical scale. Because OSIRIS is a vertical imager, a pixel number corresponds to a tangent height in an atmospheric image.

The signal, S, measured in DN, generated by a pixel, k, for an image, n, exposed

27
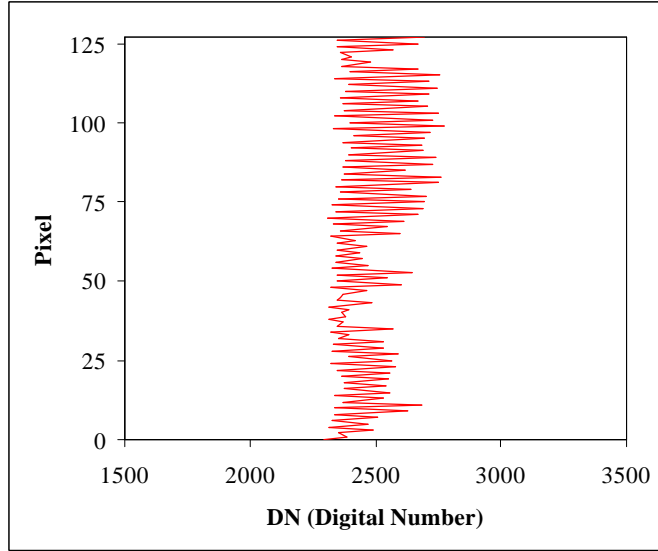
Figure 3.6: A typical dark, cold image.

in the dark, such as in the image in Figure 3.6, is

$$S(k, n) = O_i(n) + O_p(k) + S_{dark}(k, T, t), \tag{3.12}$$

where $O_i(n)$ is the signal due to the image offset that varies randomly by a few hundred DN from image to image, and is dependent on the image, n. $O_p(k)$ is the signal from the offset that varies from pixel to pixel and is constant for all images, and S_{dark} is the signal due to the dark current, unique to the pixel, k, and increases in magnitude with increasing temperature, T, and exposure time, t. S_{dark} is a negligible term in the image shown in Figure 3.6 since the exposure time, 20 ms, is very short and the temperature, -40°C, is cold.

Figure 3.7 is a plot of the difference between the image shown in Figure 3.6 and a successive dark image taken at the same temperature and with the same short exposure time. The difference has a mean of 77 DN and a standard deviation of 5 DN whereas each dark, cold image, defining the distribution of $O_p(k)$, has a standard deviation of approximately 150 DN. The deviation of the difference

28
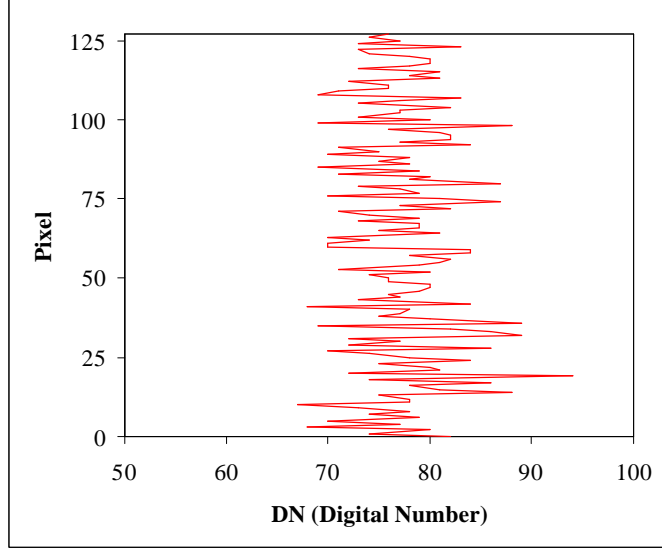
Figure 3.7: The DN difference between two succesive dark, cold images.

between the two images is random and normally distributed about the mean and is attributed to the shot noise of the detector. The non-zero mean of the difference is due to the image offset term, $O_i(n)$ in Equation 3.12. The signal in pixel, k, in the successive image, $n+1$, has a form similar to equation 3.12 such that difference, $S(k, n+1) - S(k, n)$ is

$$S(k, n+1) - S(k, n) = O_i(n+1) - O_i(n). \tag{3.13}$$

There is no dependence on the pixel offset that is constant across images. The dark current term also vanishes since it is only a function of the temperature and the exposure time for a given pixel, both of which are the same in image n and $n+1$. Successive differences between images always have a standard deviation of 5 DN across all the pixels, but have a mean that varies randomly by as much as 300 DN. However, the common dark current removal algorithm assumes that the difference between two dark images, with the same temperature and exposure time, is zero. The identified mean value in the difference, attributed to the randomly fluctuating

29

manufacturer imposed image offset, cannot simply be determined and removed when light is incident on the detector. Therefore, a modified technique that accounts for this random image offset in the presence of incident signal must be used.

3.3.2   Physical Origin of the Image and Pixel Offsets

The image and pixel offsets are features of the manufactured read-out electronics and are not documented by the manufacturer. One possible source of the image offset is that the S2 reset line in the CTIA circuit, Figure 3.3, is tied to a higher reference voltage than the S1 reset line. This would cause a positive voltage difference between S2 and S1 and lead to an image offset.

The constant relative pixel offset could be due to small non-uniformities in the values of the integrating capacitors. Therefore, when the video lines are reset, the charge stored on each of the sample-and-hold lines would vary from pixel to pixel, but would be consistent from image to image.

3.4   The Removal Technique

The difference between the readout of two pixels in an image is a parameter that does not depend on the variable image offset. For images with long exposure times or high temperatures, where the dark current term is no longer negligible, this parameter is an effective characterization of the dark current and inter-pixel offset and can be used to calibrate images that contain an optical signal.

3.4.1   Referencing the Masked Pixels

In the manufacturing process for the linear array detectors, a mask was placed over 20 pixels at one end of each array. Thus, these 20 pixels always image in the dark and provide a measure of the dark signal for images with optical signal. These masked pixels are referred to as reference pixels, and pixels that measure the incident light

are referred to as signal pixels. The DN measured by a reference pixel, r, in an image, n, of an optical source is described with the same form as in Equation 3.12,

$$S(r, n) = O_i(n) + O_p(r) + S_{dark}(r). \tag{3.14}$$

The DN measured by a signal pixel, k, when imaging an optical source contains a fourth term, $S_{ph}(k)$ (the illumination signal), as in Equation 3.15 where

$$S(k, n) = O_i(n) + O_p(k) + S_{dark}(k) + S_{ph}(k). \tag{3.15}$$

For a dark, cold image with negligible dark current, the difference between a signal pixel and a reference pixel depends only on the inter-pixel offset,

$$S(k, n) - S(r, n) = O_p(k) - O_p(r). \tag{3.16}$$

For an image of a radiative source with non-negligible dark current terms, the difference between a signal pixel and a reference pixel is the difference of Equations 3.15 and 3.14,

$$S(k, n) - S(r, n) = S_{ph}(k) + [O_p(k) - O_p(r)] + [S_{dark}(k) - S_{dark}(r)]. \tag{3.17}$$

The difference in signals described by Equation 3.17 is essentially the signal due to the incident light in pixel k plus two terms that depend on the difference between the inter-pixel offsets and the dark current characteristics of pixels k and r. It is the sum of these terms that can be characterized, as a function of exposure time and temperature, and used to remove the offset and the dark current from images that contain an optical signal.

3.4.2   The Dark Calibration Parameters

The calculation of the difference between a signal pixel and a reference pixel from a dark image with significant dark current terms is exactly the characterization term discussed above since $S_{ph}(k)$ is zero in a dark image. By choosing a single

reference pixel under the mask, Equation 3.18 can be calculated for all pixels from a dark image with a given exposure time and temperature. These values, which are functions of temperature, T, and exposure time, t, are referred to as the dark calibration parameters, $DCP(k, r, T, t)$, and are unique depending on the choice of signal pixel, k and reference pixel, r.

$$DCP(k, r, T, t) = [O_p(k) - O_p(r)] + [S_{dark}(k, T, t) - S_{dark}(r, T, t)]. \qquad (3.18)$$

Thus, when an image of an optical source is taken, at the same temperature and with the same exposure time as a set of precalculated DCP, the signal due to the incident photons can be determined by calculating the difference between a signal pixel and a reference pixel in the current image, as in Equation 3.17, and subtracting the DCP for the corresponding temperature and exposure time. The dependence on t and T is dropped in the remaining explanation as it is assumed that all references to the DCP are made for the corresponding exposure times and temperatures. The remaining signal is the signal due to the incident photons only, or

$$S_{ph}(k) = S(k, n) - S(r, n) - DCP(k, r). \qquad (3.19)$$

It should be noted that this technique also removes the image offset through the difference between the signal and reference pixel, and removes the inter-pixel offset that is contained within the DCP.

The determination of the signal due to the incident light in Equation 3.19 uses a single masked pixel as the reference. In order to minimize the noise in the calibration, a set of DCP, and therefore the signal due to the incident light, can be determined for each signal pixel and reference pixel pair. For N reference pixels, the incident light signal can then be determined as the average of N different results, each corresponding to a given reference pixel as

$$S_{ph}(k) = \frac{(N)S(k, n) - \sum_{r}^{N} S(r, n) - \sum_{r}^{N} DCP(k, r)}{N} \qquad (3.20)$$

which can be simplified to

$$S_{ph}(k) = S(k,n) - \frac{1}{N}\sum_{r}^{N} S(r,n) - \frac{1}{N}\sum_{r}^{N} DCP(k,r). \qquad (3.21)$$

Calculating the DCP for many dark images and using an average value for these parameters can further reduce the noise in the calibration process.

3.5   Calibration of Pre-Flight Dark Data

To this point, the removal technique has been discussed in terms of a given temperature and exposure time. However, in practice the imager is required to operate over a wide range of temperatures and with many exposure times. Thus it is necessary to construct a database of DCP that can be referenced for any given image temperature and exposure time. However, it is impossible to construct such a database that is complete in terms of having many dark images for all exposure times and temperatures. Hence the general effectiveness of the removal technique and the temperature and exposure time dependence of the parameters was investigated using the pre-flight data, taken with the imager in Calgary during 1998, and in Linköping, Sweden, during 2000.

3.5.1   Calgary, Canada, Data Sessions, 1998

The calibration sessions that were performed with the imager in Calgary contain a large number of dark images with the instrument in a calibration facility that had a wide range temperature control. The projected in-flight operating temperature for the image detectors was approximately -20°C; however, as the operating temperature was quite uncertain, and simply in order to fully investigate the imager characteristics, the temperatures for the data sessions were varied from -60°C to 0°C. Six different exposure times that varied from 20 ms to 1 s were used. Generally, these data sessions provide an ideal set of measurements for the dark current calibration tests.

3.5.2 Linköping, Sweden, Data Sessions, 2000

The data sessions from Linköping, Sweden, have a much smaller temperature range, near room temperature, and so are less useful for investigating the dark current than the Calgary sessions. Also, only two exposure times were used: 2 μs and 70 ms. The two microsecond data are not useful for dark current calibration because the short integration time does not allow a significant amount of dark current to collect in an image. However, the removal technique can still be evaluated in terms of its effectiveness in a worst case scenario of high temperature operation and in the removal of the image and inter-pixel offsets that are still present in the 2 μs data.

3.5.3 Odd/Even Pixel Independence

The output video lines from the CTIA of each pixel, as shown in Figure 3.3, are input to a second stage differential amplifier. However, the arrays are manufactured so that all even numbered pixels are multiplexed to a single differential amplifier, and all odd numbered pixels are multiplexed to a second differential amplifier. For this reason the even pixels and the odd pixels of each array are treated separately since the two amplifiers could have slightly different characteristics or could change differently over time.

3.5.4 Temperature Dependence of DCP

A set of DCP was calculated from the Calgary data as the average of the DCP for each even numbered signal pixel over five masked even numbered reference pixels for all images with the same exposure time. A similar set was calculated for each odd numbered signal pixel. In practice, only 10 masked pixels were used as reference as it was noticed that pixels near the illuminated side of mask are not masked effectively and light can "leak" in under the mask destroying the reference signal. The DCP calculation was performed for a temperature bin size of 0.2^oC, i.e. all temperatures falling within the 0.2 degree bins are essentially considered to be of

the same temperature. Figure 3.8 is a plot of the 1 second exposure DCP calculated for an even numbered signal pixel in Channel 3 versus temperature.

The actual meaning of the DCP is difficult to interpret as it is the difference between a dark signal and a dark reference pixel averaged over many different reference pixels. Because of the image offset that varies randomly from image to image, it is impossible to isolate and plot the dark current characteristic of a single pixel. However, the DCP as shown in Figure 3.8 still contains many interesting and interpretable features.

The plot is clearly exponential in shape. The non-zero asymptote of the parameter at low temperature is due to the inter-pixel offset and is, in fact, the average difference between the signal pixel and each of the reference pixels. As temperature increases, so the DCP increases, this indicates that the dominant source of dark current is either a reverse current (additive to the photocurrent) in the signal pixel, or a forward current (subtractive from the photocurrent) in a reference pixel. Clearly, the nature of the parameters is such that the interpretation of the physical situation, such as the direction and magnitude of the bias of each pixel, is quite complicated.

Some understanding of the situation can be gained from an investigation of the temperature dependence of the dark current. According to Equations 3.6 and 3.7, the forward dark current is a combination of diffusion current and recombination current that have different temperature dependencies. The reverse dark current is also a combination of two currents that have different temperature dependencies, the reverse diffusion current and the thermal generation current. In each case, the diffusion current is proportional to $\exp\left(\frac{E_g}{k_B T}\right)$ and the other term is proportional to $\exp\left(\frac{E_g}{2k_B T}\right)$, recalling that the sign of the exponent depends on the bias of the diode. Each set of DCP is essentially a sum of many of these terms each with different coefficients that depend on the bias and the diode properties. Figure 3.9 is a semi-log plot of the DCP shown in Figure 3.8, with the cold temperature offset removed, versus the inverse temperature in Kelvin. The slope of the best fit line

35
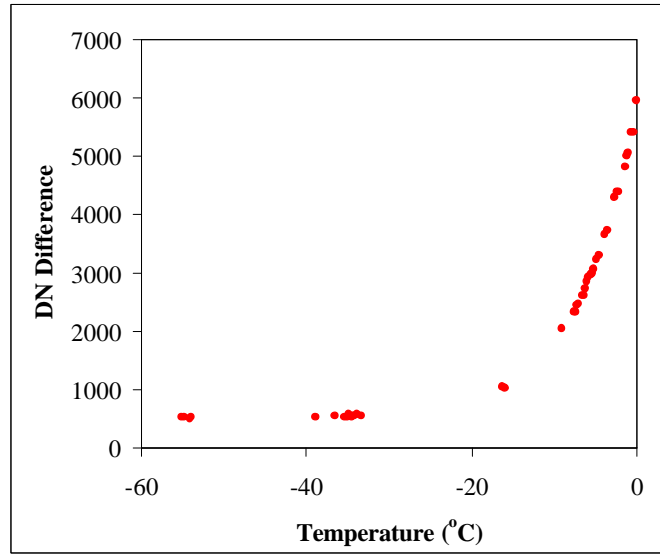
Figure 3.8: Temperature dependence of the DCP.
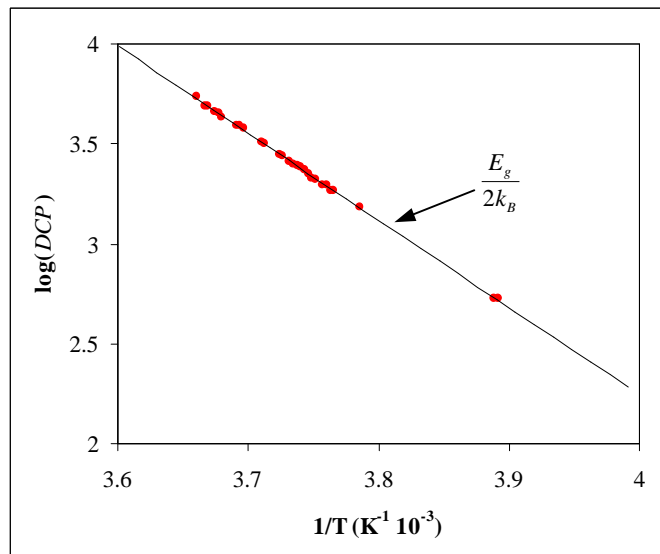
Figure 3.9: Semi-log plot of DCP as a function of $1/T$.

corresponds to 0.38 eV, almost exactly half the bandgap of InGaAs which is 0.75 eV (Kasap, 2001). A similar analysis for each pixel reveals the same $E_g/2$ dependence. This means that the diffusion term is negligible for each diode. For the reverse bias case, the dark current is dominated by the thermally generated carriers and, as in the forward bias case, the dark current is dominated by the recombination current.

Although the dark current production mechanisms for each pixel are similar, the DCP themselves are quite different in both magnitude and offset for each pixel. In fact, opposite to that shown in Figure 3.8, some parameter sets are negative since the difference between pixels could be negative for various reasons such as a forward biased signal pixel and a reverse biased set of reference pixels. Negative DCP could also result from a set of reference pixels that have a greater reverse bias than the signal pixel. However, in every case the logarithm of the absolute magnitude of the DCP, offset removed, is a linear function of $1/T$ with a slope that corresponds to $E_g/2$.

3.5.5   Calibrated Dark Images

As previously mentioned, for each exposure time in the Calgary data sessions a set of DCP was calculated as an average over many dark images with that exposure time, for the entire available temperature range, with a bin size of 0.2 ^{o}C. The parameters for each pixel were then linearly interpolated as a function of temperature for all bins that did not contain any data. To test the calibration procedure, every fifth dark image was omitted from the calculation of the parameters. These images were then calibrated using the calculated DCP. The result of a successful ideal calibration of a dark image is 0 DN beyond the instrument error for each pixel.

Figure 3.10 is a histogram of the results of the calibration of the 1 second dark images. It appears to be Gaussian in shape with a mean, μ, of 0 DN and a standard deviation, σ, of 6 DN. Thus, it appears that the errors in the technique are random and are limited to a noise floor of 6 DN. This is a factor of 10^4 below saturation
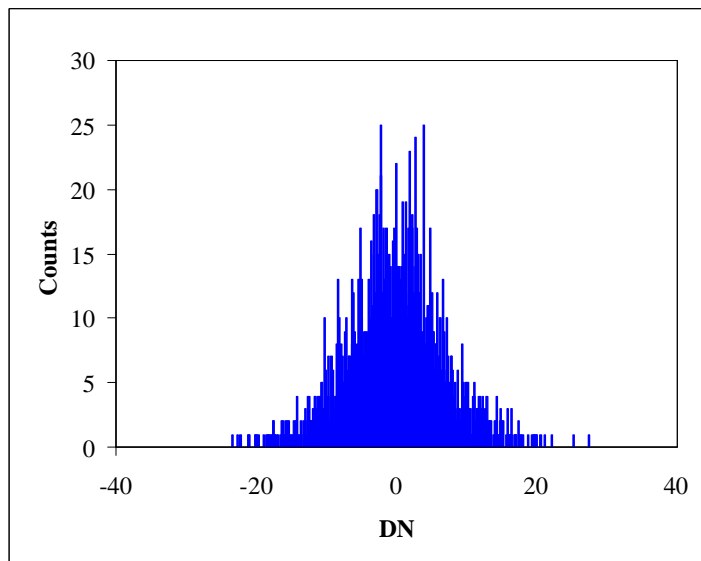
Figure 3.10: A histogram of calibrated channel 3, dark, 1 second exposure images from Calgary data sessions ($\mu = 0\ DN$, $\sigma = 6\ DN$).

and is believed to be due to the shot noise in the detectors and electronic readout noise.

The same calibration procedure was followed for all applicable exposure times taken during the Calgary data sessions, including 100 ms, 200 ms, 400 ms, and 1 s, and for all three imager channels. The results in each case were similar to those for the channel 3, 1 s exposures. Figure 3.11 is a histogram of the calibrated DN measured by all pixels in these dark images. This histogram is essentially the sum of several distributions: one for each distinct channel and exposure time although it is dominated by the longest exposure time data. Again, the error is random and attributed to shot noise with $\mu = 0\ DN$ and $\sigma = 5\ DN$.

The results of this calibration are acceptable. However, it is a limited experiment as the temperature of the images that were calibrated was very close to the temperatures used for calculating the parameters. The linear interpolation of the parameters was not robustly tested by attempting to calibrate images that fall in temperature
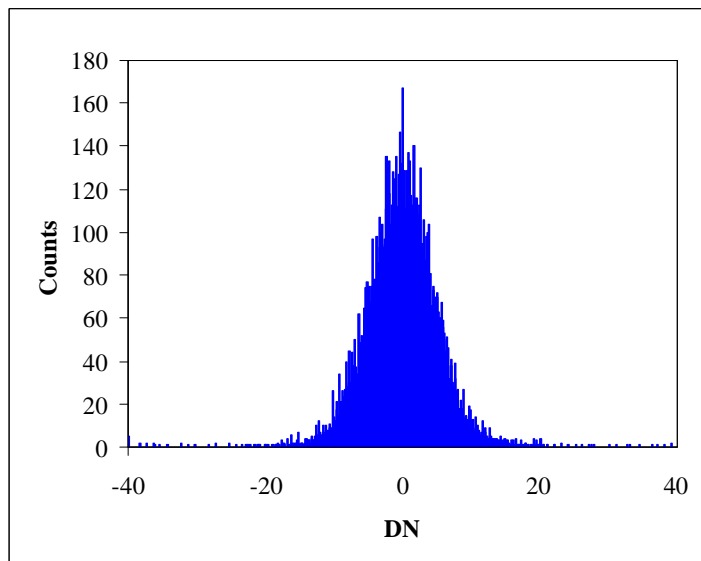
Figure 3.11: A histogram of calibrated dark images from 3 channels and 4 exposure times over a 60°C temperature range ($\mu = 0\ DN$, $\sigma = 5\ DN$).

bins that are relatively far from the bins that contain the DCP calculated directly from images. However, it is a realistic test in that the operating temperature range of the satellite experiment does not depart significantly from the range where dark calibration data is available. Also, during flight, there is much opportunity to collect large amounts of dark calibration data for the actual operating range.

A similar analysis was performed for all of the data taken in Linköping. As previously stated, these data are all taken at room temperature and are composed only of 2 μs and 70 ms exposure times. At longer exposure times, the dark current saturates the detector. In calculating the DCP for this data set, it was necessary to increase the temperature resolution of the parameters since a small change in temperature, at these high temperatures, corresponds to a large change in the dark current. The bin size used was 0.01^{o}C.

Figure 3.12 is a histogram of calibrated channel 3, 2 μs exposure time data. Because the exposure time is so short almost no dark current could accumulate. Each
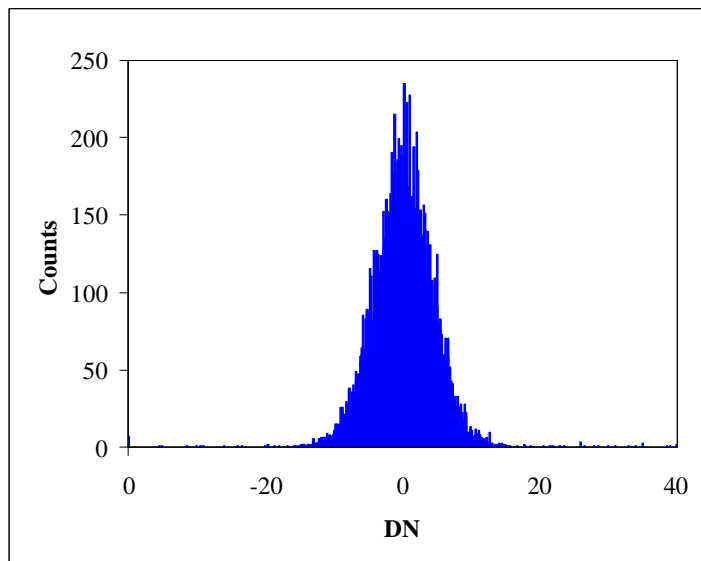
Figure 3.12: A histogram of calibrated Linköping 2 μs dark images near room temperature ($\mu = 0\ DN$, $\sigma = 7\ DN$).

of these images is composed of almost entirely image and inter-pixel offset. However, the same DCP calculation and removal algorithm was employed and the histogram of the calibrated images is a Gaussian shape with $\mu = 0\ DN$ and $\sigma = 7\ DN$. This again verifies the removal technique and agrees with the previous estimates of the shot noise.

Figure 3.13 is a histogram of calibrated channel 3, 70 ms data. The histogram is again a Gaussian, with a mean of 0 DN. However, the standard deviation is 16 DN. This is expected since the shot noise increases with temperature because more thermally generated carriers are created in a given time. Thus, it is advantageous to operate the detector at lower temperatures in order to limit the shot noise, even though the dark current removal seems to be effective at high temperatures.
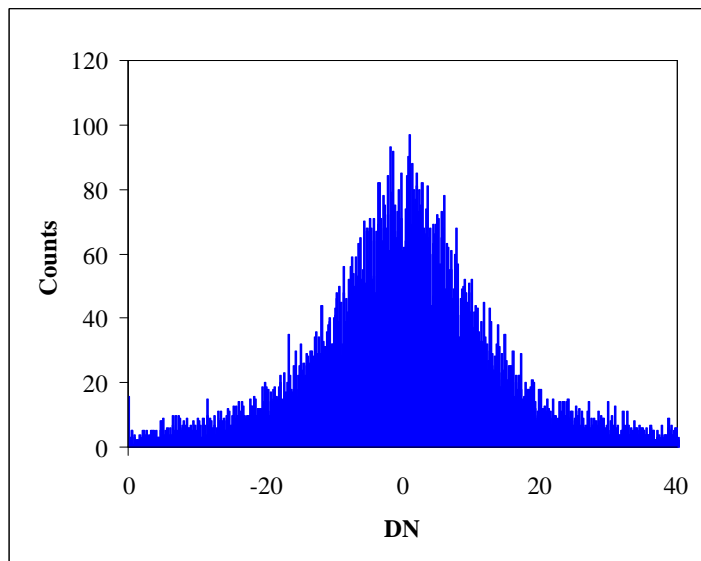
Figure 3.13: A histogram of calibrated Linköping 70 ms dark images near room temperature ($\mu = 0 \; DN$, $\sigma = 15 \; DN$).

3.6 Other Removal Techniques

There are several other techniques, all based on the same difference principle, that can be used to remove the dark current and the offsets. The basic difference between the techniques is how the different exposure times and temperatures are handled.

A second removal technique that was implemented characterized the DCP for a long exposure time, such as 1 second. The logarithm of the inverse temperature dependence of the parameters was then least squares fit to a straight line. For the calibration of an image, the parameter was multiplied by the exposure time and interpolated. This method does work quite well and calibrations with results similar to the actual removal technique employed are possible. The downfall of this technique is that the inter-pixel offset must be removed from the DCP before the semi-log regression. This requires that the offset be measured at very cold temperatures with very small exposure times so that no dark current can accumulate. As very cold temperatures are not available in space operation and there is no

continuous monitor of the inter-pixel offset, this technique is subject to a temporal variation that cannot be corrected.

3.7   Calibration of In-Flight Dark Data

Direct application of the dark calibration parameters as measured in Calgary and Linköping to in-flight data produces large systematic and random errors. This means that there have been significant changes during the time since commissioning. However, dark images with various exposure times are taken in space using the shutter system. These images have been used to calculate a new set of in-flight dark calibration parameters.

As the satellite begins a period of aeronomy data collection, the satellite is rotated so that the optic axis of the instruments is pointed toward the limb of the earth. This shift in position causes a change in the thermal equilibrium of the satellite and the temperatures of the imager detectors drop. The typical temperature change is from approximately -5°C to -20°C. The temperature remains near -20°C for the remainder of the aeronomy data collection, varying by only a few degrees. The cool down phase, which typically lasts for about 1 orbit, is an opportune time to collect dark images and check the calibration. Figure 3.14 is a histogram of a full orbit of 1500 dark images taken during a cool down phase and calibrated using dark calibration parameters calculated from in-flight measurements. The mean is 0 DN and the standard deviation is 7 DN; this is on the same order as the pre-flight measurements and demonstrates that the removal technique is valid. With a flight set of DCP, the dark current and electronic offset can be reliably removed from in-flight data, within an error corresponding to the standard deviation of a histogram of calibrated dark images.

Monitoring the DCP by calibrating successive cool down orbits has shown that the parameters do not significantly change over the period of approximately one month. However, over a period of six months an appreciable change can be de-
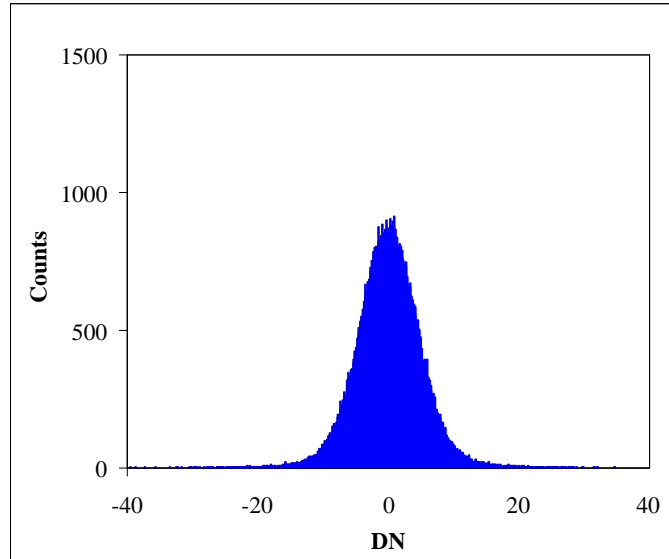
Figure 3.14: A histogram of calibrated in flight dark images of using parameters calculated from in flight measurements. ($\mu = 0$ DN, $\sigma = 7$ DN).

tected. Therefore, in processing the flight data, a new set of calibration parameters is calculated on a monthly basis. This approach provides a dark current removal error that is effectively unchanging throughout the mission. The change in the dark current removal parameters is demonstrated in Figure 3.15. The DCP for pixel 81 on channel 3, calculated from in-flight calibration data from November, 2001, is shown as a function of temperature in red, the blue curve is the DCP calculated for the same pixel from November, 2002. The systematic shift in the value of the parameter set is on the order of one hundred DN. Overall, by recalculating the parameter sets on a monthly basis over the course of the mission, the dark calibration technique performs satisfactorily and consistently on the in-flight data.

43
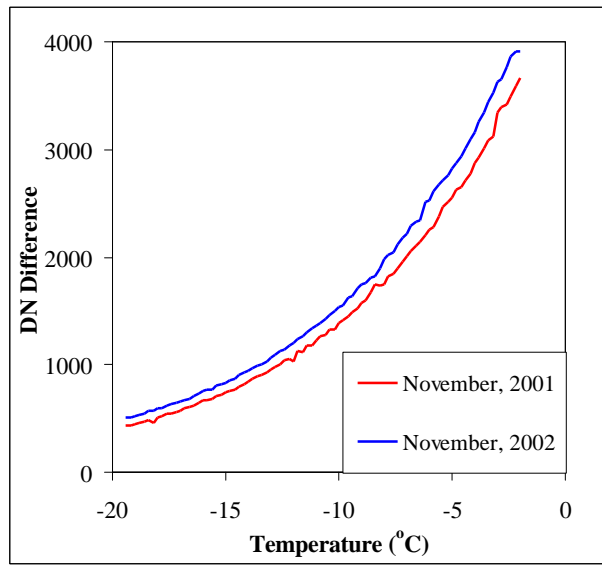
Figure 3.15: *DCP* for pixel 81 calculated from in-flight calibration data from November, 2001, and from November, 2002. There are systematic changes of approximately one hundred DN.

Chapter 4

Relative Calibration of Pixels

4.1   Introduction

In this chapter, the relative calibration of the imager pixels is presented. The analysis examines a technique that uses the pre-flight data taken in Calgary for gain calibration purposes, and investigates an apparent change in the imager gain characteristics that occurred between that time and the first in-space image. A modification of this technique has been developed in an attempt to obtain the gain calibration using only in-flight data. In addition, the measured wavelength response of the imager, on a pixel by pixel basis, is investigated to determine the extent, and origin, of the different wavelength response of different pixels and its effect on the calibration of atmospheric data. Finally, the determination of the relative look direction of each pixel, in terms of angular offset, is presented.

4.2   A Flat Field Calibration

Generally, the gain calibration of an imaging device is referred to as a "flat field" calibration. It is defined as the characterization of the relative response of different pixels on the detector to a source with uniform brightness distribution within the

field-of-view.

The flat field calibration addresses two distinct issues referred to as the *detector flat field* and the *optical flat field*. The detector flat field calibration involves the relative response of pixels on the detector for a uniform illumination of the detector area. The optical flat field calibration is a characterization of the pre-detector optical system of the instrument and is a measure of the relative number of photons incident on different pixels when a source of uniform brightness distribution occupies the entire instrument field of view.

4.2.1 Optical Flat Field

The optical system of the imager includes several baffles for stray light rejection and an aperture stop that limits the light beam in a predictable way. Vignetting occurs when the incident beam is limited in any way other than by the design of the aperture stop. This effect often occurs at high off-axis angles within the instrument field of view. The optical flat field calibration must characterize the effects of vignetting so that they can be removed in the calibration.

A vignetting analysis was performed by Ivanov (2000) who traced beams of parallel rays at various off-axis angles through a software model of the IRI system. This procedure allows the calculation of the total illumination of the detector by determining those surfaces of the system that limit the incident beam. It was found that for small off-axis angles, the aperture stop is the limiting baffle. However for high off-axis angles, near the edge of the detector that corresponds to high pixel numbers (the optical axis, the pixel aligned with the bore sight of the other instruments on Odin, is pixel 15), the entrance vein and the lens bracket limit the incident beam and decrease the signal. Figure 4.1 is a plot of the modelled signal incident on the detector, after transmission through the imager baffle system, for incidence angles corresponding to the field of view of the detector. Also shown for comparison on the same plot are uncalibrated images, one from each channel, of a

46
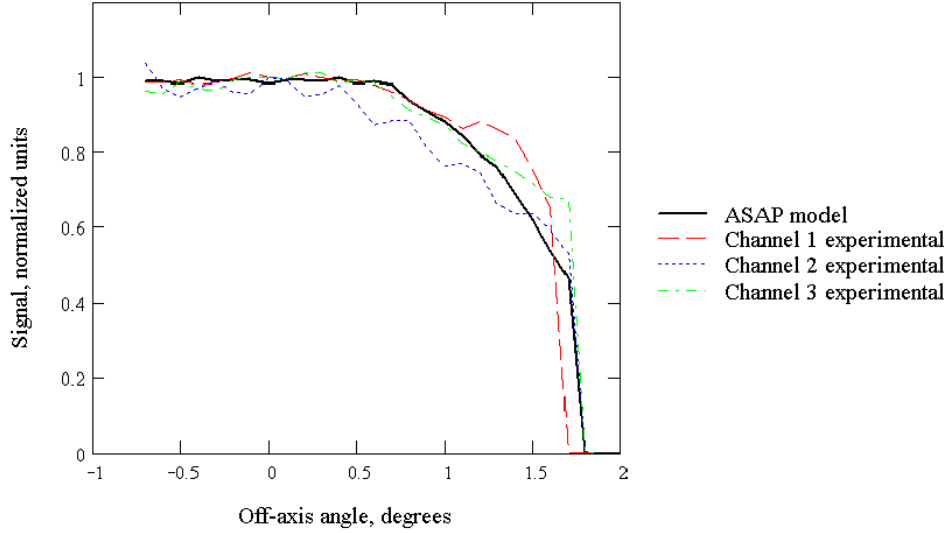
Figure 4.1: Modelled and measured instrument response for a uniformly distributed brightness source. Optical vignetting is evident at high off-axis angles. (Ivanov, 2000)

uniform brightness source taken during the Calgary pre-flight data sessions. The experimental data are in good agreement with the modelled result. In this figure, the off-axis angle is proportional to pixel number.

It is important to note that the *detector flat field* effects also modify the experimental curves so direct comparison with the model of the *optical flat field* effects is not valid. The experimental images in Figure 4.1 have been smoothed using a running average to compensate for the detector flat effects in an attempt to remove the variation between individual pixels. Ignoring the small variations over small changes in the off-axis angle, the trend of decreasing signal for high off-axis angles is obvious and of comparable shape and magnitude for each channel.

47

4.2.2 Detector Flat Field

Due to small variations in the manufacturing processes, each pixel has a quantum efficiency, an associated gain stage in the CTIA (Capacitive Trans-Impedance Amplifier) shown in Figure 3.3, and a filter response that varies slightly from each of the other pixels. The calibration determines the response of each pixel for a uniform illumination of the detector area so that any variation in the conversion process from incident photons to DN, on a pixel to pixel basis, can be corrected.

Figure 4.2 is plot of Lambertian source images for all three channels. It uses the same data as that shown in Figure 4.1; however, these data have been corrected for dark current and electronic offsets only and no averaging or normalization has been performed. The small scale structure, i.e. the relative differences between neighboring pixels (those over a small range of incidence angles), is caused by the different response of each pixel to a uniform brightness; the characterization and removal of this structure is the detector flat field. It is important to remember that the odd and even numbered pixels on each channel are multiplexed through separate amplifiers in the second gain stage. The difference between the amplifiers is evident in the images shown in Figure 4.2. This is especially true for channel 2, where the odd pixels have a response that is systematically lower than the even pixels. This odd/even effect is a major element of the *detector flat field* calibration.

Indistinguishable from the response of the photodetector and amplifier is the transmission of the interference filter that is mounted directly on to the detector area. Some of the difference in response between pixels could be due to the varying response of the filter to slight changes in incidence angle. However, this effect should vary smoothly over the detector area, like the optical flat field, and not cause a large variation in the response of adjacent pixels. It is demonstrated in this thesis that the assumption of a uniform filter transmission for all pixels on a given channel is the current best effort.
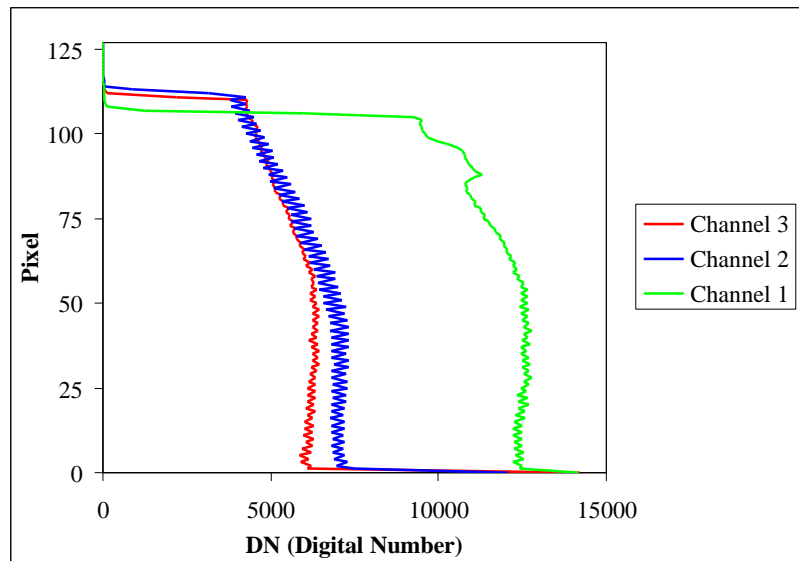
Figure 4.2: Lambertian source images from each channel. The *detector flat field* effect is evident in the small scale structure superimposed on the smoothly varying *optical flat field* effect that increases the signal towards lower pixel number.

4.3 Pre-Flight

4.3.1 Filter Shape Measurements

The pre-flight calibration data from Calgary includes images that measure the shape of the wavelength dependence for each channel. As it is impossible to isolate the interference filter from the photodiode array, these measurements characterize both the effect of the filter shape and the wavelength dependence of the diode quantum efficiency.

A monochromator output was collected by an integrating sphere and then focused independently on each channel so that images could be recorded for several wavelengths near the central wavelength. For example, with the monochromator in the field of view of channel 2 exposures were made at wavelengths between 1243 nm and 1283 nm in 2 nm increments. Because the optical power output of the source

was very low, the exposure time was greatly increased to 300 seconds. However, the long exposure times caused some pixels to underflow because of dark current. In order to minimize this effect, the temperature of the detectors was lowered to $-40^{o}C$ and held at a constant temperature for all exposures. As several dark images were taken during the same session, the dark current and electronic offsets could be removed from the monochromator images for each pixel in all three channels. Figure 4.3 is a plot of the normalized filter shapes for all pixels in channel 2. It is readily apparent that the shape of the wavelength dependence varies between pixels in the same channel.

Some variation of the filter shape between pixels is expected because the interference filter, mounted directly in front of the detector array, is sensitive to the incident angle and each pixel of the linear array is at a physically different location. The variation of the filter shape due to the incident angular dependence should have a smooth trend across the detector. Figure 4.4 is a plot of the integrated filter shapes (area under the filter) for channels 2 and 3. On each channel, a smooth trend is clearly visible across the detector although there is an overlying inter-pixel structure. This is especially true in the channel 2 data; the inter-pixel structure has an odd/even dependence with the even pixels having an integrated filter shape that is systematically lower than the odd pixels. The actual normalization process is sensitive to random structure near the peak of the filter shape that could affect the integrated area. However, because the peak of each filter shape has been independently normalized to 1.0, any effects from the separate amplification of the odd and even pixels are removed. The systematic difference visible in Figure 4.4 is possibly due to the physical offset of the odd and even pixel columns on the focal plane surface of the detector chip. The remaining inter-pixel structure is attributed to noise in the measurement and variations across the filter area and the photodetector wavelength response. The integrated filter shapes for channel 1 have characteristics similar to those shown in Figure 4.4, but are not included on this plot because they are centered around 40 nm, which reflects the wider band-pass.
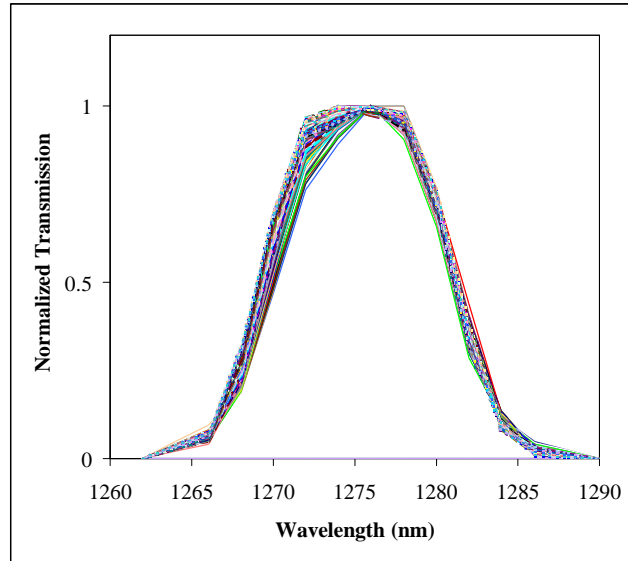
Figure 4.3: Filter shapes for all pixels on channel 2. Each pixel is shown with different coloured line. The shape for each pixel is independently normalized to a peak value of 1.0.
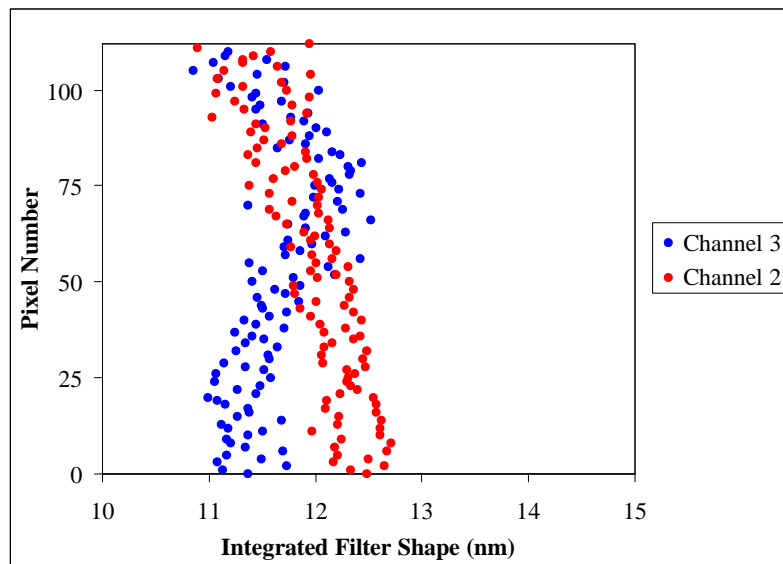
Figure 4.4: The integrated filter shapes (peak normalized to 1.0) for channels 2 and 3. A smooth trend and inter-pixel structure is visible on both channels.

51

4.3.2 Temperature Dependence of the Gain

A Lambertian source has a uniform brightness that occupies the entire field of view of the imager. A set of Lambertian source images from the Calgary pre-flight data sessions were taken at detector temperatures between 0^oC and -60^oC, with various exposure times. Hundreds of images were taken for each channel; however, the source brightness was such that many of the images contain saturated signal. Only those images that do not contain any saturated pixels were used in the analysis of the temperature dependence of the electronic gain.

The dark current and electronic offsets were removed in the normal way (Chapter 3) and each image was normalized by exposure time. The temperature dependence of the gain is shown in Figure 4.5, which plots the signal measured by pixel 64 (channel 2) as a function of temperature. The data are from 81 images, and four distinct temperature ranges are visible by the four clusters of data. A temperature dependence of increasing gain with decreasing temperature is clear. A similar analysis of many pixels reveals that the strength (i.e. slope) of this dependence is different for different pixels.

Figure 4.6 shows the slope of the best fit straight line for all pixels on channels 2 and 3. The odd and even pixels on each channel are plotted in separate colours in order to show the independent behavior of each set. For channel 2, the temperature dependence is systematically weaker for all odd pixels. However, for both the odd and even sets, there is a distinct maximum in the strength of the dependence near the middle of the array. For channel 3, a systematic difference in the *shape* of the trend across the detector is different for the odd and even sets without a clear offset of either the odd or even set. The maximum in slope for this channel occurs at a different point on the array for each data set.

A difference in the gain characteristic of the odd and even set that is constant across the array can be explained by a difference in the temperature dependence of the gain of the two separate amplifiers for each channel. However, the variation of the temperature dependence across the array that causes the maximum near the
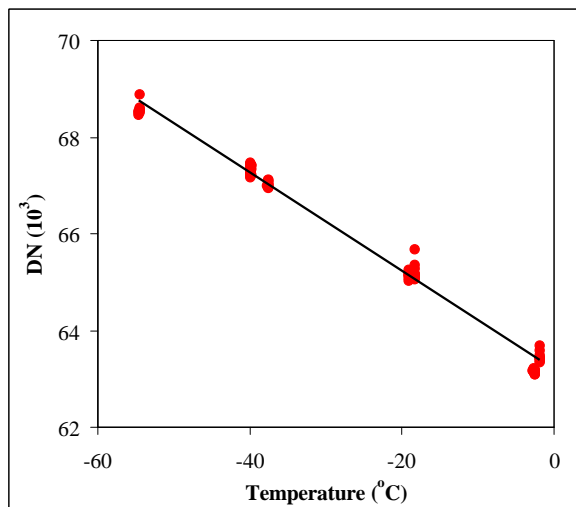
Figure 4.5: Temperature dependence of the gain: Lambertian source data from pixel 64 on channel 2 calibrated for dark current and offsets, and normalized to 1 second exposure time.
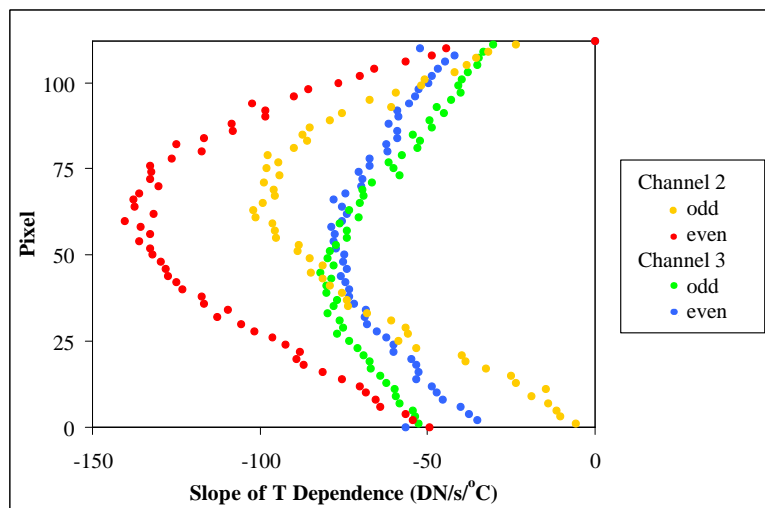
Figure 4.6: The slope of the best fit line of the electronic gain temperature dependence of each pixel for channels 2 and 3. Note that the even and odd pixels on each channel have a distinct temperature characteristic.

middle pixels is not a characteristic of the read-out electronics. It is believed that this is due to a change in the in the filter as the temperature decreases. At lower temperatures, the pixels near the edges of the array have physically fewer incident photons than the pixels near the middle. This is expected as interference filters typically have a temperature dependence that decreases the central wavelength and the magnitude of the peak transmission as temperature decreases. This effect would be compounded by pixels at non-normal incidence angles that already suffer from a shifted central wavelength and decreased peak transmission.

4.3.3   Description of Technique

For each pixel, k, the imager provides an observation, O_k, of the differential brightness of the incident optical signal, $B_s(\lambda)$, integrated across the passband of the channel filter, $f(\lambda)$,

$$O_k = \tau_k \int B_s(\lambda) f(\lambda) \mathrm{d}\lambda. \tag{4.1}$$

In Equation 4.1, τ_k is a constant, different for each pixel, that converts from incident photons to Digital Number, and includes the characteristics of the optical system, i.e. the detection area and the solid angle of the field of view. The units of the observations, O_k, are DN, the units of the differential source brightness are $\frac{\mathrm{photons}}{\mathrm{cm}^2 \ \mathrm{s} \ \mathrm{nm} \ \mathrm{sterad}}$, and $f(\lambda)$ is dimensionless. Appropriately, τ_k has units of $\frac{\mathrm{DN}}{\frac{\mathrm{photons}}{\mathrm{cm}^2 \ \mathrm{s} \ \mathrm{sterad}}}$ where the wavelength dependence has been absorbed in the integration.

The observations must always take on this integral form because the source brightness, $B_s(\lambda)$, the atmospheric emission, varies with time and location.

The goal of the imager is to make an instrument independent measurement of the source brightness across the passband. The flat field calibration, coupled with the absolute calibration, is the calculation of the set of τ_k's. However, a decision must be made about the nature of the calibrated data product. Equation 4.1 assumes that the filter shape, $f(\lambda)$, is the same for all pixels on a channel. If this is the case

then the number of photons incident on each photodetector in the linear array is the same for a uniform illumination of the aperture so that the calibrated image is *flat*. However, as noted in Section 4.3.1, the shape of the filter, and the area under it, changes across the array. Therefore, the number of photons incident on each pixel after transmission though the filter is different. Thus, the channel filter, $f(\lambda)$, in Equation 4.1 should be replaced with a filter shape unique to each pixel, $f_k(\lambda)$,

$$O_k = \tau_k \int B_s(\lambda) f_k(\lambda) d\lambda. \tag{4.2}$$

The consequence of the difference between Equations 4.1 and 4.2 is important. With a filter shape that is different for each pixel, the image of a uniform illumination across the aperture is no longer flat. If the differential source brightness, $B_s(\lambda)$, is constant over the wavelength range of the filter passband, it can be taken out of the integral and Equation 4.2 becomes:

$$O_k = \tau_k B_s \int f_k(\lambda) d\lambda. \tag{4.3}$$

In this case, the image for uniform illumination has the same shape as the integrated normalized filter shapes shown in Figure 4.4 but scaled by the intensity of the incident signal. The disadvantage in this is that the interpretation of a single image becomes difficult because the measurement from each pixel is only relative to measurements from other pixels through the relation of their filter shapes. Images of the atmospheric brightness height profile would not be smooth, but would contain structure corresponding to the integrated filter shape. In a sense, the imager no longer makes an instrument independent measure of the source brightness within the field of view since each pixel is essentially treated as its own instrument. The alternative is to assume an average filter shape for all pixels on a channel and attempt to calibrate out the variation of filter shape between pixels. However, this has serious implications for the interpretation of the atmospheric emission data. Because a molecular emission is a band spectrum that changes with emission temperature, the "band capture fraction", or percentage of the emission that is transmitted through

55

the filter, changes as a function of the emission temperature, which is a function of height in the atmosphere. As an illustrative example, as a pixel scans up in tangent height it measures a smooth brightness profile as the brightness of the emission changes; some change in the brightness profile is also due to a change in the band capture fraction as the emission temperature changes with tangent height. The neighboring pixel also measures a smooth brightness profile through the scan in tangent height; however, this profile has a slightly different shape because of the change in band capture fraction with emission temperature is different. The undesirable result is that when two successive images, with a different optic axis tangent height, are aligned in tangent height, the profiles will have systematic differences. The decision of the Odin/OSIRIS science team is that the Level One Data Product, a term referring to the fully calibrated imager measurements, will assume an average filter shape for all pixels on a channel such that individual profiles maintain a smooth shape. The normalized filter shapes measured in Calgary will be provided as a service to users or the Level One data who wish to proceed in the scientific interpretation of the atmospheric measurements.

If it is assumed that pixels in a channel have the same filter shape, Equation 4.1, then a Lambertian source (LS), which has a uniform brightness across the entire field of view, can be used to characterize the effects of both the *optical flat field* and the *detector flat field*. The calculation of the τ_k's is then straight forward since the integral, $I = \int B(\lambda) f(\lambda) \mathrm{d}\lambda$, is the same for all pixels. For simplicity, and because we are not currently concerned with the absolute magnitude of the response but with the relative response between pixels for a uniform brightness in the field of view, the assumption is made that $I = 1 \frac{\text{photon}}{\text{cm}^2 \text{ s ster}}$. Therefore, by rearranging Equation 4.1, the set of τ_k's can be calculated from the set of observations of the LS, $O_{k(\text{LS})}$, as

$$\tau_k = \frac{O_{k(\text{LS})}}{1 \ \frac{\text{photon}}{\text{cm}^2 \text{ s sterad}}}. \tag{4.4}$$

After each τ_k has been calculated, the flat field calibration can be applied by dividing each pixel's observation of an unknown source by the respective τ_k (see

Equation 4.1).

$$\int B_s(\lambda)f(\lambda)\mathrm{d}\lambda = \frac{O_k}{\tau_k}. \tag{4.5}$$

It should be noted that in Equation 4.5, the final product of the calibration does not provide any information about the wavelength dependence, or shape, of the source brightness. All information is effectively lost by the integration of the signal across the passband. The final product is simply the number of photons per second, within the normalized passband of the channel, incident on the detector.

4.3.4   Application: Calgary Data Sessions

The temperature dependence of the Calgary LS data was least squares fitted as illustrated by the trend line in Figure 4.5. The set of τ_k's for each channel was calculated according to Equation 4.4 for temperature bins of 1°C. The resulting database was then applied to the LS data in a self-calibration. Figure 4.7 shows the histogram of the results of the self-calibration. The plot contains all data from all pixels for channel 2. The other channels have similar results. The histograms are all centered at 1.000 and have a half width of less than 0.010, this corresponds to a random error in the flat field of less than 1%. This uncertainty is acceptable as it is consistent with the random instrument error and is stable across the detector.
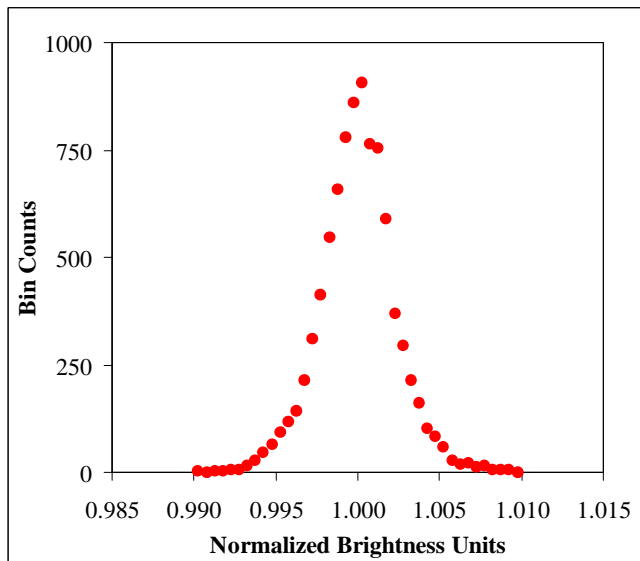
Figure 4.7: Histogram of Channel 2 Lambertian source data for all pixels after the flat field calibration has been applied.

4.4 In-Flight

4.4.1 Application: Flight Data

The set of flat field parameters, τ_k's, that were calculated from the Calgary LS data with an average filter shape for each channel were applied to the first in-flight images of the $O_2(a^1\Delta_g)$ limb profile without apparent success. Figure 4.8 shows a plot of a limb image of the $O_2(a^1\Delta_g)$ emission profile measured in channel 3 after the dark and flat field calibrations have been applied. A plot of the modelled emission as measured in the limb through the channel filter is also shown. The systematic offset of the odd and even numbered pixels in the measured image is clearly evident; the even pixels measure a signal that is significantly lower than the adjacent odd numbered pixels. The cause of the odd/even offset is not understood at this point; it should have been corrected with the calibrations. It is difficult to determine if the odd/even effect has occurred since the launch of the satellite, or if the effect could

58
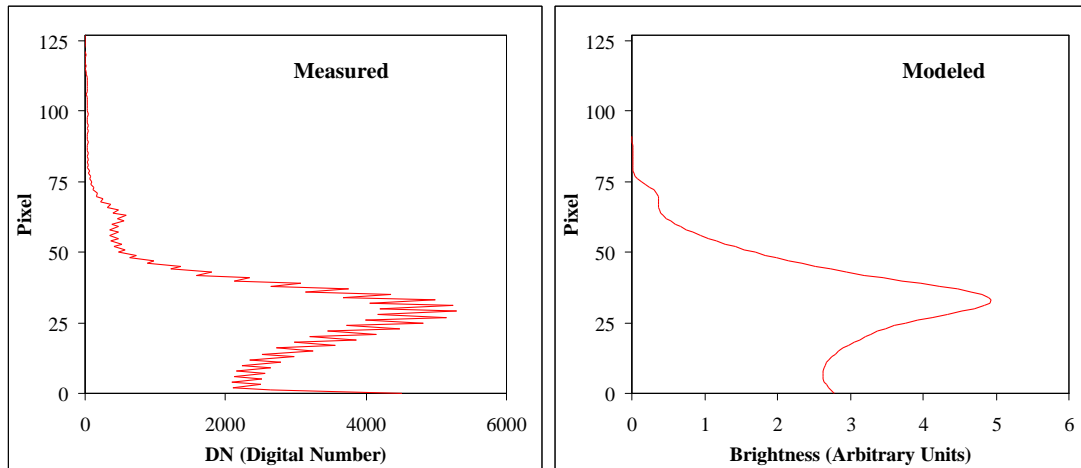
Figure 4.8: An typical imager channel 3 limb profile after dark calibration and flat field with pre-flight parameters compared to a modelled $O_2(a^1\Delta_g)$ limb image.

be understood with a better pre-flight calibration data set. Possible causes include temperature gradients in the electronics, a shift in the detector or filter plane, or temperature dependent filter shapes.

It is interesting to note that the calibration of data from channel 1, which measures an OH emission and Rayleigh scattered sunlight at 1.53 μm and has a much wider filter, does not produce any noticeable odd/even effect. If the effect is due to the filter then channel 1 would be much less sensitive to small changes.

4.4.2 A New Technique

In the best case scenario, the imager would be re-calibrated with a Lambertian source to determine if a change in the calibration had indeed occured and, if so, the cause of the observed odd/even effects. This is obviously not possible with an in-flight satellite instrument. However, in the middle of the daytime, the peak of the $O_2(a^1\Delta_g)$ emission at 50 km altitude has a relatively constant brightness over a period of hours. As OSIRIS scans through a range of tangent altitudes in the limb, each pixel of the imager scans through the emission peak. A new set of τ_k's can be

determined by assuming that during a scan all pixels measure the same brightness of the peak with the same filter shape. In a sense, this approximates the Lambertian source conditions of the laboratory. Figure 4.9 is a plot of the average of several measurements made by each pixel in channel 3 as it scans the peak of the daytime $O_2(a^1\Delta_g)$ emission. This figure also includes a plot of a pre-flight Lambertian source image from the Calgary data sessions such as that shown in Figure 4.2. For direct comparison, the brightness of the signals has been arbitrarily normalized in both data series to the signal in pixel number 1. The shape of the signal from the odd pixels of the detector appears to have remained very similar to the Lambertian source image. However, the even pixels are affected by a systematic offset below the odd pixels and have also changed their relative shape on the detector. This is especially true in the trend towards low pixel number. A second interesting feature of this comparison is that the small odd/even offset effect that is observable in the pre-flight data (see Section 4.2.2) is opposite to the effect in the flight data in that it is the odd pixels that measure a signal that is consistently below the even pixels. The cause of the inconsistency in not known; the obvious possibilities are a confounding effect of the two amplifiers that read out the odd and even pixels separately, and the path difference through the interference filter between odd and even pixel columns in the detector focal plane. Even though it cannot be explained at this time, an attempt at a reliable calibration must still be made.

Using the emission peak brightness, a new set of τ_k's was calculated in the same manner as for the Lambertian source data. Figure 4.10 is a plot of the same measured limb image shown in Figure 4.8 except that the flat field calibration is now performed with the measured emission peak scan parameters. This result agrees very well with the the modelled result shown in Figure 4.8. These emission peak parameters provide equally acceptable results when applied to the flight data images for both of the singlet delta channels.

The temperature dependence of the gain (Section 4.3.4) cannot be effectively investigated with these flight parameters as the imager temperature on the spacecraft
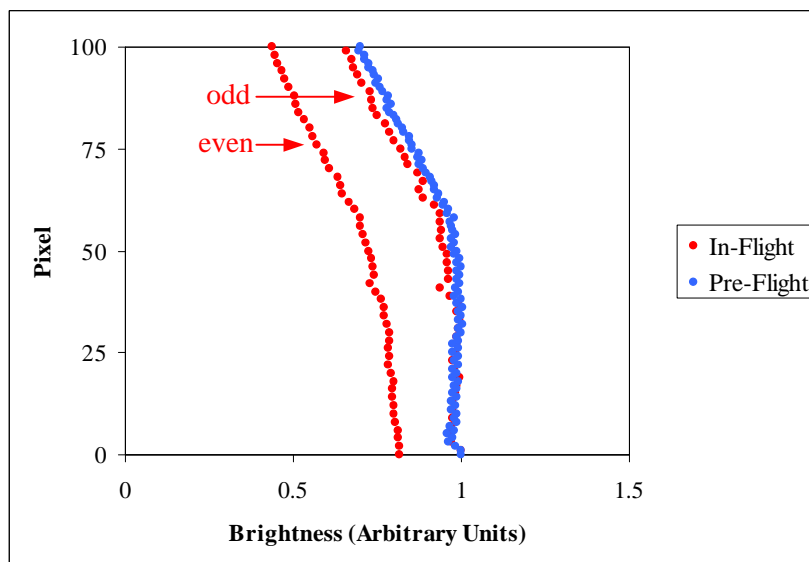
Figure 4.9: The average of several in-flight measurements of the emission peak by each pixel (red) compared to the pre-flight Lambertian source data (blue).
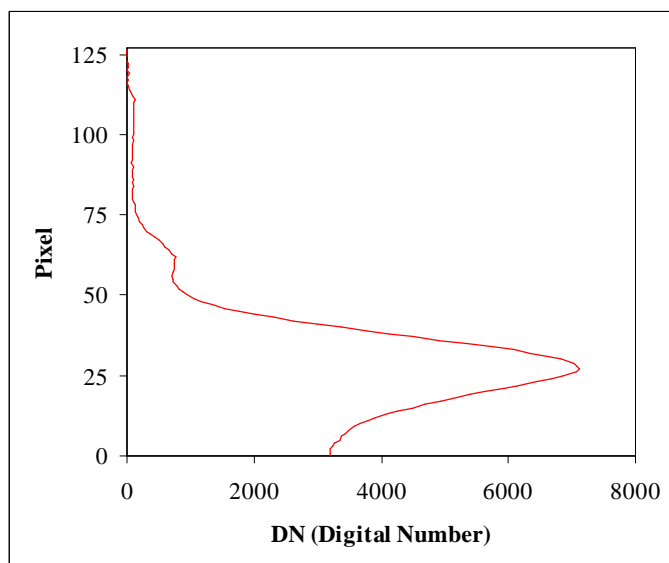
Figure 4.10: The measured limb image shown in Figure 4.8 after dark calibration and flat field correction with peak scan parameters calculated from flight data.

varies by only a few degrees during the satellite's progression through changing illumination conditions; of course, the best conditions for sampling the peak emission for the construction of the new flat field parameters always occurs during the middle of the daytime in the same part of the orbit and therefore at approximately the same temperature. However, because the instrument temperature varies by only a few a degrees, the temperature dependence of the gain is less critical.

4.4.3   Effect of Filter Shape Variation

The assumption a single filter for all pixels on a channel (Section 4.3.3) yields smooth profiles like those shown in Figure 4.10. However, the interpretation of successive images at different optic axis tangent heights is difficult as all pixels have a filter shape that deviates from the mean filter assumed for the entire channel. The effect of the variation of filter shape can be investigated through the temperature dependence of the band emission using data calibrated with in-flight flat field parameters.

As the satellite nods while it travels along the orbit track, a single pixel scans through a range of tangent heights in successive images. A neighboring pixel scans through the same heights but offset in each image by 1 km. Each pixel measures a smooth brightness profile as a function of tangent height; however, due to the slight difference in filter shape, the band capture fraction for each pixel is not exactly the same. This means that as the atmospheric temperature changes with height, the band capture fraction changes differently for the two pixels.

Depending on the scientific mode of the satellite, the optic axis nods over a different range of tangents heights. In the largest nod range mode, the optic axis scans from 10 km to 100 km in approximately 2 minutes with 1 second exposures taken every 2 seconds. This corresponds to a vertical resolution of about 1.3 km. Figure 4.11 shows the $O_2(a^1\Delta_g)$ emission height profile for a single scan as measured by 5 different pixels. The pixels are all near the optic axis (pixel 15) end of the array since pixels at the other end of the array do not measure the same height range.

However, as shown in Figure 4.4, the integrated area of the filter corresponding to these pixels varies by approximately 6%. Figure 4.12 shows the ratio of the profiles measured by these pixels (4, 17, 35, 46) to the profile measured by pixel 16. For all heights between 10 km and 75 km the deviation of the profiles is less than 2%. Pixel 17 shows the least variation in height profile and no systematic structure with height. The other pixels, especially 46 and 35, display a trend in the ratio that may correspond to a change in band capture fraction with temperature that is different than pixel 16 due to the variation in filter shape. However, since the overall variation in measured signal is less than 2% and the area of the normalized filter shapes varies by 6%, the effect of changing band capture fraction with height is small. It should also be noted that there is a lack of distinction between even and odd pixels. Above 75 km, the ratios of the height profiles varies more drastically from unity. However, as the atmosphere is much more dynamic and the signal is much smaller it is difficult to determine how much of the difference in height profile between pixels is actually due to the variation in filter shape, or rather a change in the atmosphere between images, or simply lower signal to noise ratio.

4.5   Relative Look Direction

In September, 2000, the alignment and field of view of OSIRIS was measured at the CESR facility in Toulouse, France. In a set of measurements designed to measure the IRIS field of view, the CESR collimator beam was moved in a horizontal scan across the detector at two different locations on the linear array. As the optics needed to be uncovered for these experiments, the clean room conditions allowed only two scans to be made. However, these two scans allow the calculation of the angular vertical field of view of each pixel based on the relative motion of the two scans of the collimator beam for the assumption that all pixels are symmetric. Lloyd (2000) has calculated the vertical field of view as 1.186' per pixel for all channels. Given this information and the attitude solution for the satellite, which determines
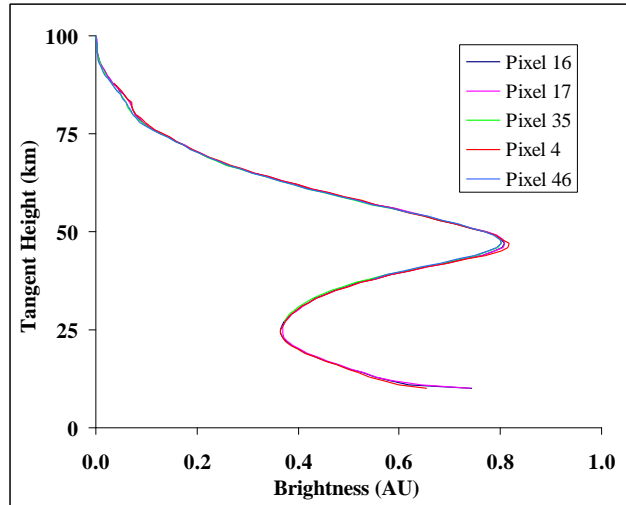
Figure 4.11: $O_2(a^1\Delta_g)$ emission height profiles from a single satellite scan as measured by five different pixels on channel 3.
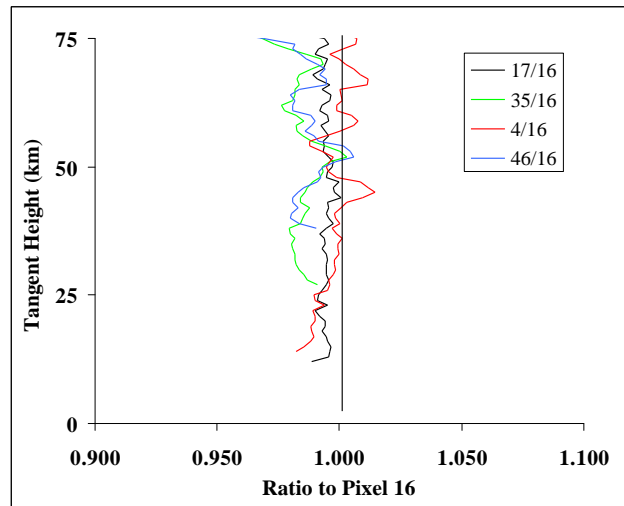
Figure 4.12: The ratio of the height profile measured by each pixel in Figure 4.11 to the profile measured by pixel 16. The deviation of the profiles is less than 2% for all pixels between 10 km and 75 km.

the tangent height of the optic axis pixel, the tangent height of all pixels in an image can be determined.

Using the derived angular field of view (FOV) successive images can plotted as a function of tangent height and image number. Figure 4.13 is a plot of six scans of atmospheric data comprising 500 images. The tangent altitude of the optic axis scans between approximately 10 km and 70 km as shown in black. In this scan mode, a 1 km bin centered at 60 km tangent height is always sampled by some pixel on the array no matter what the tangent height of the optic axis. The brightness measured for these six midday scans at 60 km, which should be relatively constant during the middle of the day, is shown in red in Figure 4.13. The structure of the scan is clearly evident and is the result of an incorrect vertical angular field of view.

Degenstein (2002) has investigated the vertical angular field of view using several hundred in-flight scans of $O_2(a^1\Delta_g)$ channel data. A large portion of the emission height profile, including the peak of the emission, used for the calculation of the in-flight flat field parameters is measured by all of the pixels on the array during a scan of the optic axis. During this scan time, which lasts for only a few minutes, the altitude of the peak remains constant. By varying the field of view and tracking the location of the peak in all pixels, an angular spread between pixels which produces the least variation in the location of the emission peak can be determined. Degenstein has calculated a vertical FOV of 1.203' per pixel for channel 2 and 1.204' per pixel for channel 3. These vary by approximately 15% from the value determined by Lloyd (2000). Channel 1 FOV cannot be determined with this method because the OH emission is not stable over the course of even a few minutes.

In order to investigate further the field of view of the imager, an in-flight experiment was made. The satellite was pointed off-track and several horizontal scans were made so that the image of Jupiter crossed the detector at different pixel locations. The image of Jupiter has an angular size that is approximately the same size as a single pixel. A method similar to that used to analyze the Toulouse data was used to determine the vertical FOV from the Jupiter scans. (Lloyd, 2002). The

results are:

<div style="text-align:center">

Channel 1: 1.193' per pixel

Channel 2: 1.205' per pixel

Channel 3: 1.206' per pixel

</div>

These values agree with the values calculated by Degenstein (2002) to within 1%. The brightness at 60 km calculated according to the Jupiter scan data is also shown in Figure 4.13. As expected, the brightness is relatively constant with almost no structure due to the nod of the optic axis. The relative calibration of the imager pixels can be performed with confidence.
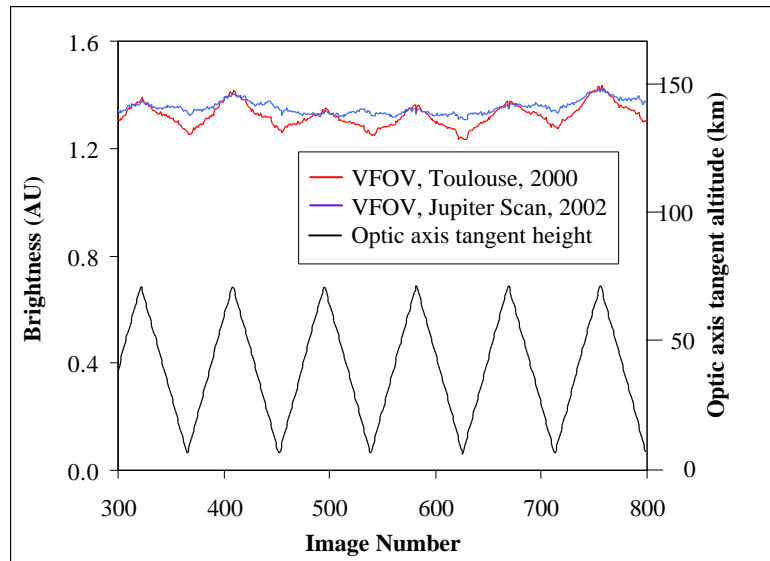
Figure 4.13: Six scans of data. The tangent altitude of the optic axis is shown in black. The limb emission measured at 60 km tangent height is shown for the angular vertical field of view calculated from both the Toulouse measurements and the Jupiter scans.

Chapter 5

Stray Light Removal

5.1 Introduction

This chapter presents an analysis of the stray light signal in the IR imager. A summary of previous modelling work (Ivanov, 2000) is shown to provide an understanding of the mechanisms involved. The stray light signal in the atmospheric images is investigated, and a technique for the characterization and removal of the effects is developed and implemented.

5.2 Stray Light Model Analysis

In the model of an ideal imaging system, a parallel beam of light, at some angle to the optic axis within the field of view of the system, is imaged on to the detector area as a geometric point. All other incidence angles beyond the field of view are rejected. However, in a real system, some non-zero signal from outside the field of view illuminates the detector; in addition, the image of a parallel in-field beam is spread over a finite area on the detector. These effects, which degrade the image quality, are essentially due to two processes: the scattering of light from surfaces that are not ideally smooth or have non-zero reflectivity, and the diffraction of off-

axis light at the entrance aperture. Stray light from diffraction effects is common in instruments that suffer from the geometry of measuring a source that is in close proximity to a secondary source that is much brighter than the primary source. By Huygen's principle, off-axis light from the bright secondary source, that is beyond the field of view of the instrument, forms sources of spherical secondary waves at the aperture that can interfere constructively into the field of view. Figure 5.1 is a simplified diagram of Huygen's principle. The standard unit for the characterization of these effects is the Normalized Detector Irradiance, or NDI. It is defined as the ratio of the detector brightness averaged across the detector area to the brightness of a parallel off-axis beam at the entrance aperture in a plane normal to the line of sight to the source.

Using the ray tracing software model of the imager, Ivanov (2000) calculates the NDI due to scattering of off-axis light in the optical system. As the amount of processing time required for the calculation of diffraction due to multiple aperture limiting surfaces is prohibitive, the effects of diffraction for a single imaging element system can be represented by the Fraunhofer far-field approximation of diffraction at a circular aperture. The mathematical formulation of Huygen's principle for scalar optical disturbance, U_p, at observing point p, using the far-field approximation is

$$U_p = C \int e^{ikr} \mathrm{d}A, \tag{5.1}$$

where A is area of the aperture, $k = 2\pi/\lambda$ is the wave number, C is a complex constant, and r is the distance from p to the aperture. Equation 5.1 assumes that the angular spread of light both from source to aperture and from aperture to p is small. The geometry used in the application of Equation 5.1 to a circular aperture is shown in Figure 5.2. For an aperture radius, R, and an integration variable, y, the area element is $2\sqrt{R^2 - y^2}\,\mathrm{d}y$ and the phase factor is $e^{k(r_o + y\sin\theta)}$, where $r_o = r$ for $y = 0$. Therefore, Equation 5.1 becomes

$$U_p = Ce^{ikr_o} \int_{-R}^{+R} e^{iky\sin\theta}\, 2\sqrt{R^2 - y^2}\,\mathrm{d}y. \tag{5.2}$$

68
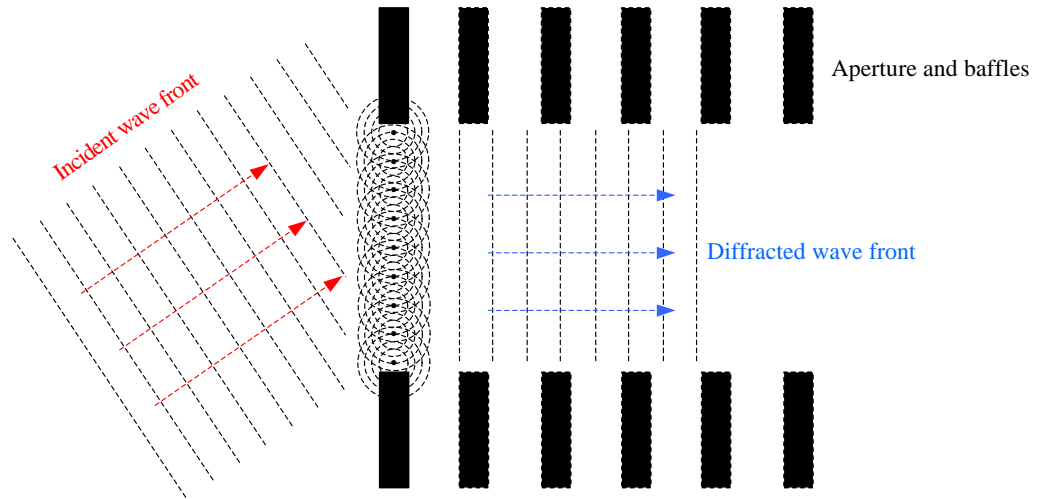
Figure 5.1: Huygens principle: light from a bright secondary source not in the field of view can be diffracted into the field of view through the constructive interference of spherical secondary waves at the aperture.
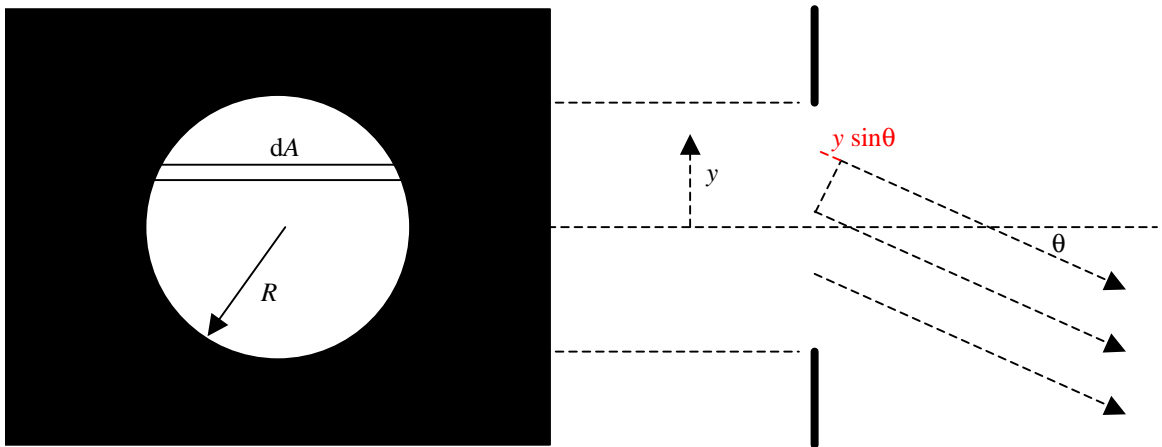
Figure 5.2: Fraunhofer diffraction geometry for a circular aperture.

69

The result of this integral is the familiar Airy function that can be written in terms of the first order Bessel function, $J_1(\rho)$, where $\rho = kR\sin\theta$. Since the intensity, I, of the diffraction pattern is proportional to the square of U_p, the ratio of the intensity of the pattern to the intensity of the source at $\theta = 0$, I_o, is:

$$\frac{I}{I_o} = \left[\frac{2J_1(\rho)}{\rho}\right]^2.$$ (5.3)

The fringes of the diffraction pattern have a half-angle period of approximately

$$\theta_o = 1.22\frac{\lambda}{d}$$ (5.4)

where d is the diameter of the aperture. This corresponds to an angular spread in the fringes of approximately one tenth of a pixel. Therefore, the individual fringes are not be visible in an image as a single pixel samples many fringes; however, a shape due to the diffraction pattern is still superimposed on the image.

For large off-axis angles, $\theta \gg \theta_o$, $J_1(\rho)$ can be approximated and the Airy function averaged over the fringes. This gives the following equation for the NDI as a function of off-axis angle in terms of the focal length of the lens, f, (Caldwell and Gray, 1997),

$$\text{NDI}(\theta) = \frac{\lambda d}{4\pi^2 f^2 \theta^3},$$ (5.5)

where the inverse cube dependence on θ approximates the envelope of the fringe pattern.

Figure 5.3 is a plot from Ivanov (2000) of the diffraction/scattering modelling for off-axis angles up to 45°. Clearly the diffraction term dominates the stray light for all off-axis angles. The large spike in the stray light contribution for small off-axis angles within the field of view is due to a lens bracket that is both an illuminated object and a critical object. The bracket is only illuminated for angles between 0.5^o and 2.5^o as it is shielded by the baffling for angles greater than 2.5^o and by the aperture stop for angles less than 0.5^o. Residual scattering at higher off-axis angles is mainly due to scattering from baffle tips that have a finite width, approximately
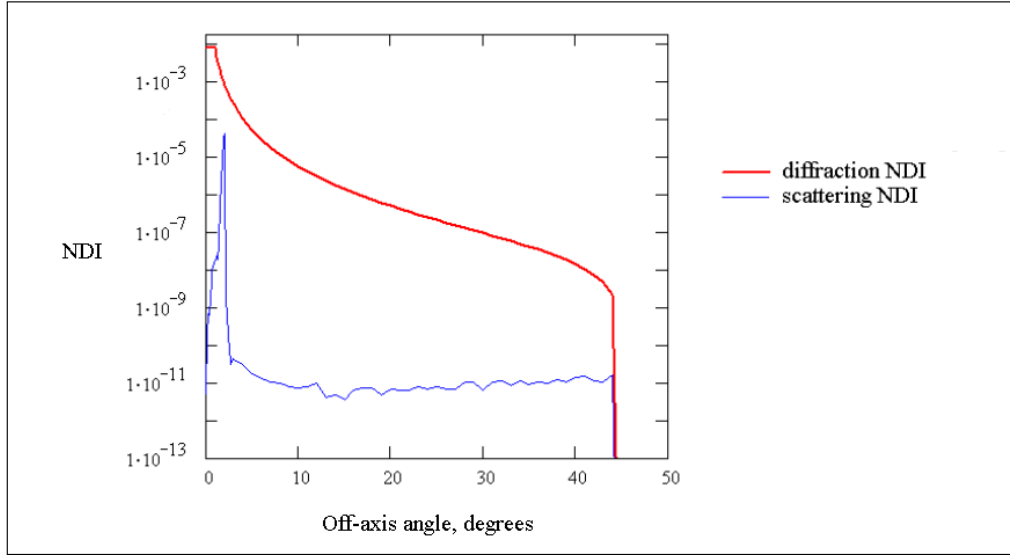
Figure 5.3: Normalized Detector Irradiance (NDI) for off-axis angles of incidence due to scattering and diffraction. (Ivanov, 2000)

50 microns. Overall, the maximum stray light due to scattering and diffraction from any off-axis angle, even within the field of view, is less than 10^{-2} NDI. It is important to note that this analysis does not provide any information about the shape of the signal on the detector area, it only gives the total average illumination of the detector area as a function of the off-axis angle to the source. Of course, the total stray light signal in the imager will be the sum of these two effects and other smaller terms.

5.3 Evidence of In-Flight Stray Light

The signal due to atmospheric emission and atmospheric scattering decreases with increasing tangent height. For the $O_2(a^1\Delta_g)$ channels the signal above 100 km tangent height is nearly zero. Figure 5.4 is a plot of a typical midday $O_2(a^1\Delta_g)$ tangent height limb profile, similar to the calibrated profiles shown in Chapter 4;

71

however, instead of plotting the brightness as a function of pixel number it is plotted as a function of tangent height central to the sampling pixel's field of view. The signal evident above approximately 100 km is due to stray light as it does not originate within the field of view of these pixels. Figure 5.5 is a two dimensional field plot of all images in a single orbit, for the same $O_2(a^1\Delta_g)$ channel, as a function of tangent height. The colour scale indicates the brightness of the signal in arbitrary units. The stray light signal above 100 km is evident throughout the daytime images. The variation in magnitude is probably due to the brightness of the underlying Earth's surface. Whether it is due to scattering or diffraction is difficult, if not impossible, to determine. The off-axis source brightness, i.e. the Earth's surface, varies along the satellite track and covers a large continuous range of off-axis angles. However, even without a full understanding of the source and cause of the in-flight stray light signal, a characterization of the effect can be attempted in order to remove the stray light from the calibrated data product.

5.4   Characterization and Removal of Stray Light

In both modelling and measurement, the stray light signal on the detector area is characteristic of the source brightness and the off-axis angle. All of the pixels that measure at a tangent height above a minimum altitude where the atmospheric signal is negligible provide a measure of the stray light signal. If the shape of the stray light is known across the entire detector, these high altitude pixels can be used to determine the magnitude of the stray light so that it can be removed from the entire image. Thus, a requirement of the imager stray light removal algorithm is that there are some pixels that measure the magnitude of the stray light in the absence of a direct atmospheric signal.
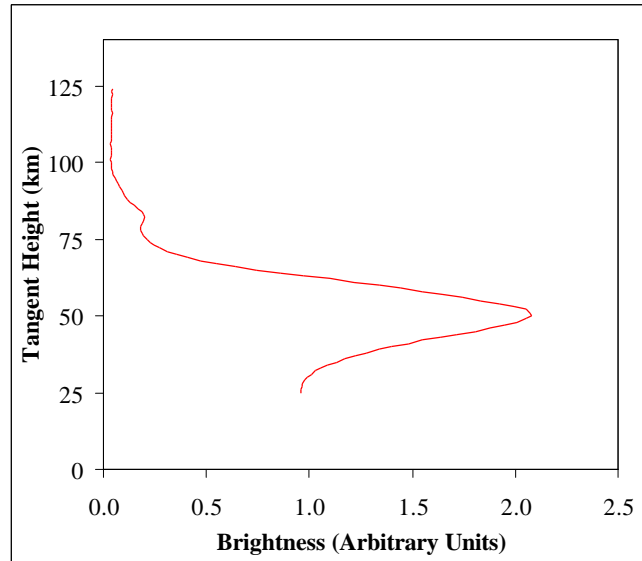
Figure 5.4: Typical midday $O_2(a^1\Delta_g)$ tangent height limb profile after dark calibration and relative gain correction. Stray light signal is evident at high tangent altitudes where the signal due to atmospheric emission and atmospheric scattering is essentially zero.
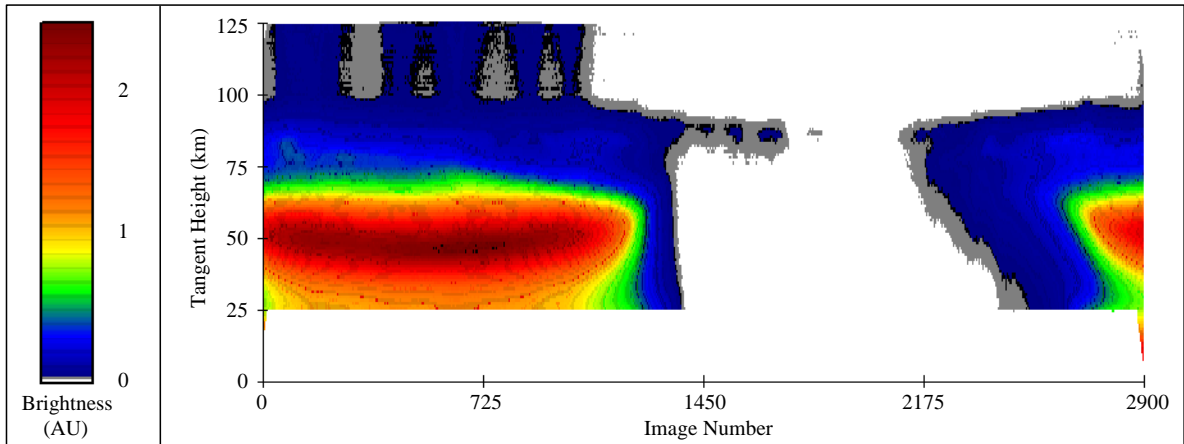
Figure 5.5: Typical $O_2(a^1\Delta_g)$ tangent height limb images for one orbit. The colour scale indicates brightness. Solar illumination conditions vary throughout the orbit; midday occurs near image 600 and midnight occurs near image 1900. Stray light is evident above 100 km with varying magnitude throughout the daytime.

5.4.1 Stare Mode and Nod Mode

By its design, the OSIRIS imager measures approximately 100 simultaneous lines of sight over 100 km in the vertical. Therefore a single image contains all of the information for a 100 km tangent height profile with 1 km resolution. However, the other instruments on board Odin, such as the OSIRIS spectrograph, have a single line of sight that is aligned with the optic axis of the imager. This means that each exposure only measures at one tangent height (or integrated over the range of tangent heights associated with the angular field of view of the single line of sight). In order to retrieve information for many tangent heights, i.e. to reconstruct a height profile, the satellite scans through a range of tangent heights while several images are collected. This scanning operation is referred to as the "nod mode" and operation at a constant tangent height (the preferred imager operation) is referred to as the "stare mode".

5.4.2 Characterization of the Stray Light Signal

As noted in Section 5.4, all pixels with a tangent height above a maximum atmospheric signal altitude make a direct measurement of the stray light signal. The shape of the signal on the detector area is a function of the off-axis angle of the source and the magnitude of the signal is a function of the brightness of the source. The nod mode of the satellite provides an opportunity to measure the shape of the stray light on the detector area for a range of off-axis angles.

The optic axis of channel 1 is pixel 15 and pixels 16 through 127 have lines of sight with tangent points higher in the atmosphere. Channel 1, centered at 1.53 μm, measures the nighttime OH Meinel band emission and in the daytime measures Rayleigh scattered sunlight and a very weak OH emission. Stray light is not an issue at nighttime because there is no secondary source, i.e. the Earth is not illuminated. In the daytime, the 1.53 μm Rayleigh scattered signal and the weak OH emission is negligible above 60 km so that all pixels above 60 km measure a signal that is

dominated by stray light.

In nod mode, images are taken at many tangent heights that correspond to various secondary source off-axis angles. As the brightness of the Earth's surface, the cloud cover, and other influencing factors change with time along the satellite track, the same off-axis angle at two different times may correspond to a significantly different secondary source brightness. By normalizing the magnitude of the stray light, the shape of the signal can be characterized as a function of off-axis angle, or practically and simply as a function of the optic axis tangent height.

Figure 5.6 is a plot of the shape of the stray light signal for channel 1 averaged over several orbits of nod mode data (i.e. many thousand images) for the assumption that all signal above 60 km in the daytime is due to stray light. Daytime is defined in this scenario as a solar zenith angle of less than 93°. In order to normalize the magnitude of each stray light image, a factor that indicates the brightness of the off-axis is needed. The factor used to produce the characterization is the sum of the signal in all pixels above the minimum atmospheric signal (MAS) tangent altitude, i.e. the lowest tangent altitude that contains no atmospheric signal from emission or scattering within the field of view.

As shown in Figure 5.6, the range of optic axis tangent heights covered was from approximately 0 km to 100 km. For the line of sight of the optic axis closest to the Earth, the smallest number of pixels (82 to 107) measure at tangent altitudes above 60 km (the MAS tangent altitude) and therefore measure a signal dominated by stray light. It should be noted that pixels 108 through 127 are under the dark current mask. When the optic axis is pointed at tangent altitudes above approximately 75 km, all pixels on the array are above 60 km and so measure only stray light. This variation in the number of pixels that measure stray light as a function of altitude causes the the triangular shaped area of "missing" data in the bottom left of the plot. In practice, the stray light signal extends to lower looking pixels where the data is "missing", but it cannot be characterized through direct measurement because at lower tangent altitudes, the signal contains light from atmospheric scattering and

emission within the field of view as well as stray light.

In order to remove the stray light effectively from any given image, the shape of the stray light across the *entire* detector must be known. Figure 5.7 shows the result of an extrapolation of the shape of the stray light shown in Figure 5.6. The triangular shaped area of missing data has been filled in by extrapolating the value at the lowest known tangent height for a given pixel to lower tangent heights where the shape cannot be measured.

To demonstrate the extrapolation process, Figures 5.8 and 5.9 are respectively vertical and horizontal cross sections of the 2D field plot shown in Figure 5.7. Figure 5.8 is a plot of the stray light in pixel 64 as a function of the optic axis tangent height. The data points associated with the blue curve are measured values while the red curve is an extrapolation of the stray light signal at the lowest known tangent height as a constant for lower unmeasurable tangent heights. Figure 5.9 shows the shape of the stray light on the detector as a function of pixel number for an optic axis tangent height of 50 km. Again, the blue curve represents the measured values and the red curve is the extrapolation of the shape from the lowest measured tangent height. The irregular nature of the shape of the scattered light both as a function of off-axis angle (optic axis tangent height) and pixel number makes it difficult to extrapolate the measurements down to tangent heights that include atmospheric signal. However, by extending the lowest measured value of stray light down into the lower looking pixels, the removal of the stray light can be performed smoothly across the entire detector for an image that contains an atmospheric signal from within the field of view.

The characterization technique described above for channel 1 was also applied to several thousand images of in-flight data from the singlet delta channels (2 and 3) with similar results. However, there is a distinct difference between the characterization for the OH channel and the $O_2(a^1\Delta_g)$ channels as the MAS altitude for the $O_2(a^1\Delta_g)$ emission is much higher, near 105 km. This means that the extrapolated area begins at higher tangent heights so that there are fewer pixels that measure

76
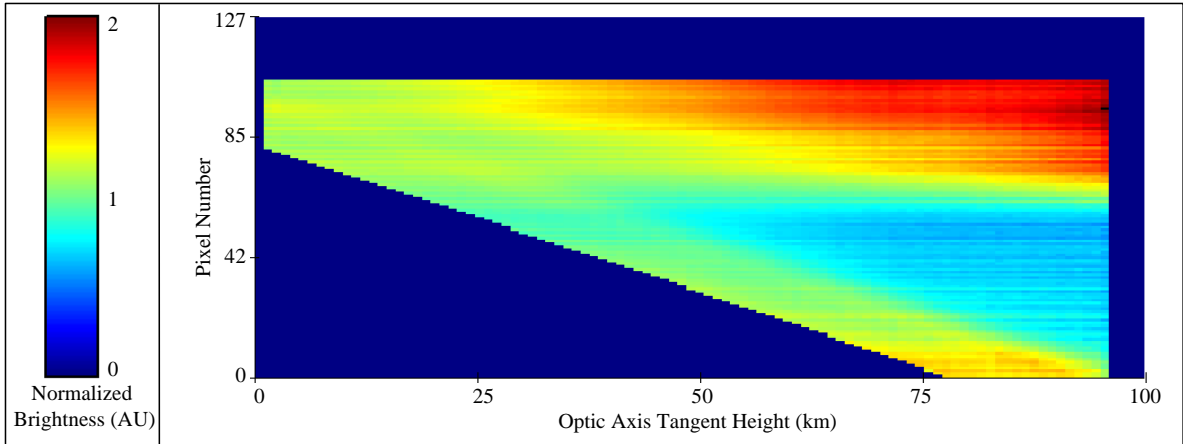
Figure 5.6: Characterization of the *shape* of the stray light signal on the detector as a function of optic axis tangent height and pixel number.
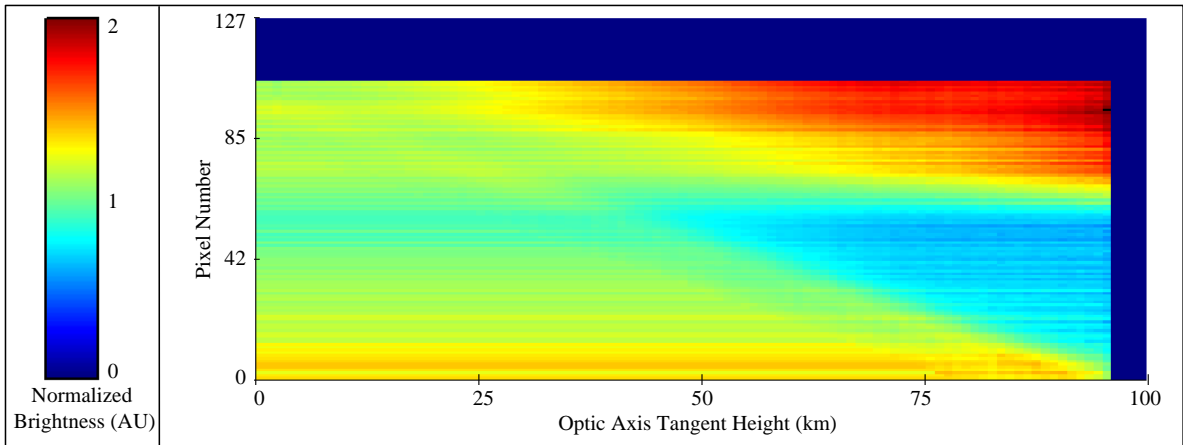
Figure 5.7: Extrapolated characterization of the *shape* of the stray light signal on the detector.
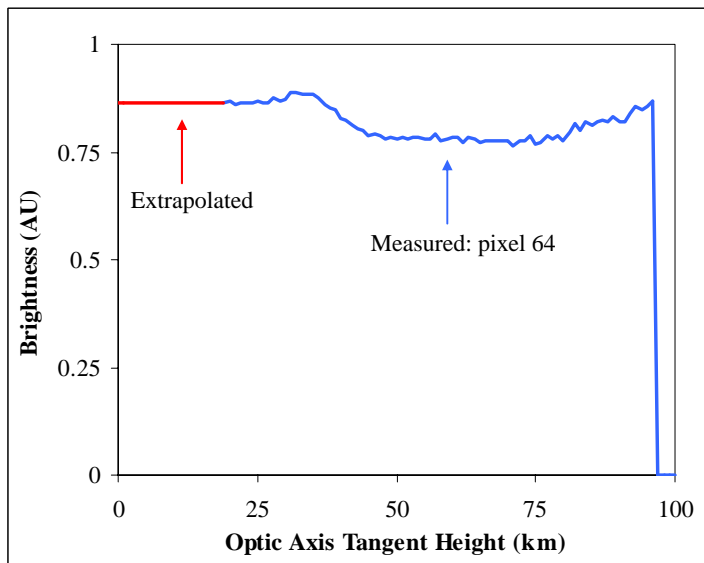
Figure 5.8: The measured and extrapolated stray light for pixel 64 as a function of optic axis tangent height, i.e a horizontal cross section of Figure 5.7.
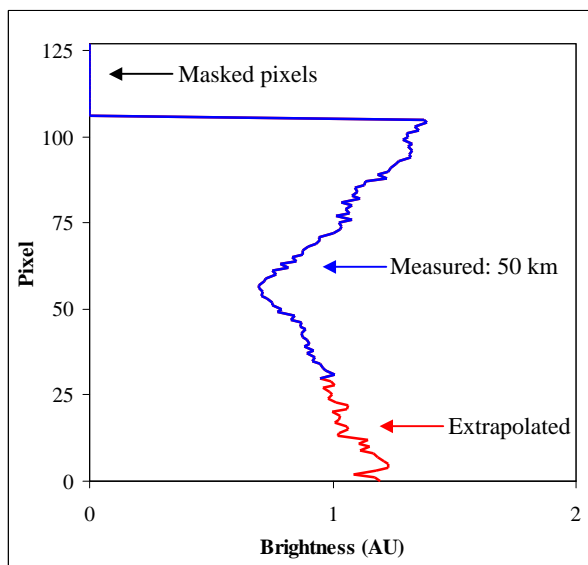
Figure 5.9: The measured and extrapolated normalized shape of the stray light on the detector for optic axis tangent height of 50 km, i.e. a vertical cross section of Figure 5.7.

above the MAS for a given optic axis tangent altitude. A particular in-flight data set was taken especially for the characterization of the stray light. This set includes scans up to very high tangent altitudes so that the entire array measures above the MAS altitude. Thus the shape of the stray light on the detectors can be measured and extrapolated down to lower tangent heights. In a fortunate coincidence, the optic axis of channels 2 and 3 are at pixel 20, 5 pixels higher than for channel 1. This means the entire detector arrays on channels 2 and 3 measure approximately 5 km higher for the same optic axis tangent height. The analysis produces shape characterizations that are similar to those shown in Figures 5.6 to 5.9 for channel 1; however, for processing reasons, the removal of the stray light occurs after the dark calibration, and before the relative gain correction, so that the stray light characterizations for channels 2 and 3 contain the odd/even effect.

5.4.3   The Removal Technique

The characterization of the shape of the scattered light extrapolated across the detector as a function of the optic axis tangent height (Figure 5.7) can be used to remove the stray light from an in-flight image. However, as the characterization provides only information about the shape of the scattered light, the magnitude of the stray light signal must be determined on an image by image basis. The normalization procedure for the determination of the shape, outlined in Section 5.4.2, determines the average signal in all pixels above the MAS altitude and divides all pixels measuring the stray light signal above the MAS altitude by that value. A similar method can be applied to the shape characterization of an in-flight image. The extrapolated shape of the stray light on the detector that corresponds to the image optic axis tangent height is multiplied by the average of all pixels above the MAS altitude for that image. The scaled shape is then subtracted from each pixel in the image.

It is important to note that this method requires that there are some pixels

that measure at a tangent height that is above the MAS altitude. Technically, the removal could be performed with only a single pixel above the MAS altitude; however, because it is an averaging technique, the random noise associated with a measurement is decreased if more pixels are used.

5.5   Application to Flight Data

5.5.1 $O_2(a^1\Delta_g)$ Channels

Figure 5.10 is a plot, similar to Figure 5.4, that shows a typical $O_2(a^1\Delta_g)$ tangent height limb profile from midday plotted in red. The stray light removal algorithm has been applied to this profile using a characterization of the shape from above 105 km and magnitude normalization parameters from those pixels in this profile that measure above 105 km. The corrected profile is shown in blue. The second plot in this figure is a re-scaling of the same profile for tangent heights above 70 km where the mesospheric molecular emission and the solar scattering signal are dominated by the stray light. The features that are due to the $O_2(a^1\Delta_g)$ emission such as the secondary mesospheric peak and the decrease of the signal with increasing tangent height are clearly evident; the increasing signal above 105 km due to stray light has been removed. Figure 5.11 is a plot of the entire orbit of images shown Figure 5.5 after stray light removal. It is readily apparent that the stray light above 105 km is no longer evident.

It is difficult to gauge qualitatively the effectiveness of the stray light removal. The removal algorithm is based on the requirement of zero signal for high tangent altitudes, i.e. those altitudes above the MAS altitude where the measured signal is only due to stray light. Therefore, if the removal is effective, the signal above the MAS will be zero, within the random noise of the system for all images. Figure 5.12 is a histogram of the residual signal in those pixels above the MAS altitude for all images of the images shown in Figure 5.11. It appears Gaussian in shape, centered
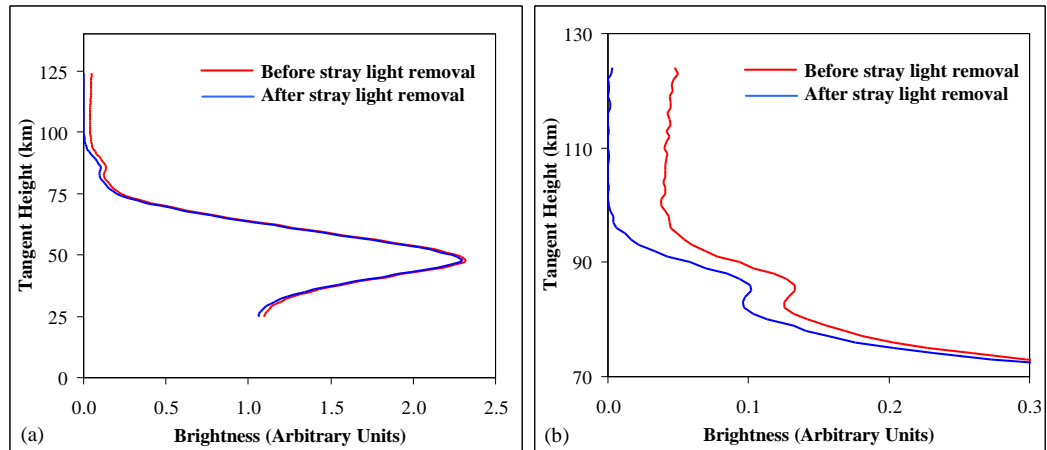
Figure 5.10: (a) The typical midday $O_2(a^1\Delta_g)$ tangent height limb profile shown in Figure 5.4 before and after the stray light removal. (b) A re-scale of the same image shown in plot (a) to demonstrate the effect of the stray and the effectiveness of the removal at high tangent altitudes.
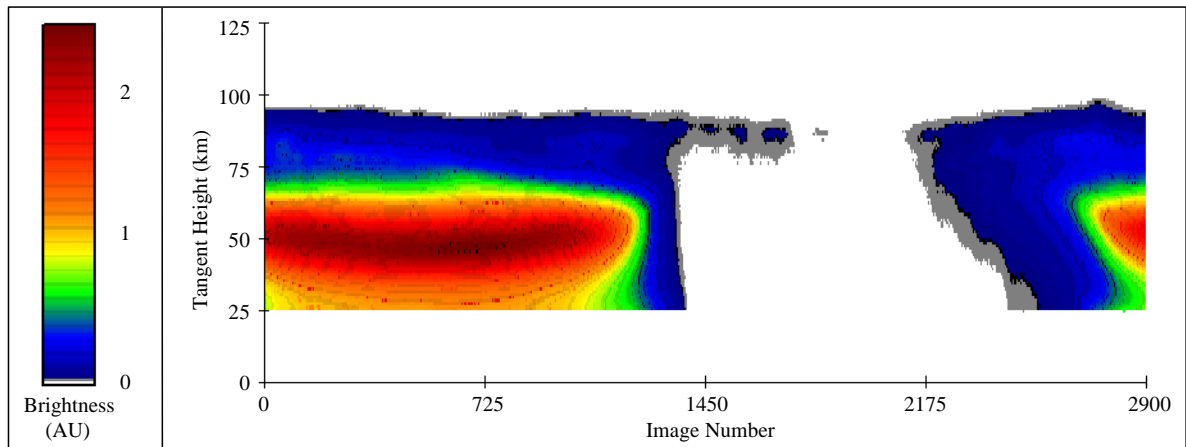
Figure 5.11: $O_2(a^1\Delta_g)$ tangent height limb profile images for the same orbit shown in Figure 5.5 after the stray light removal has been performed.
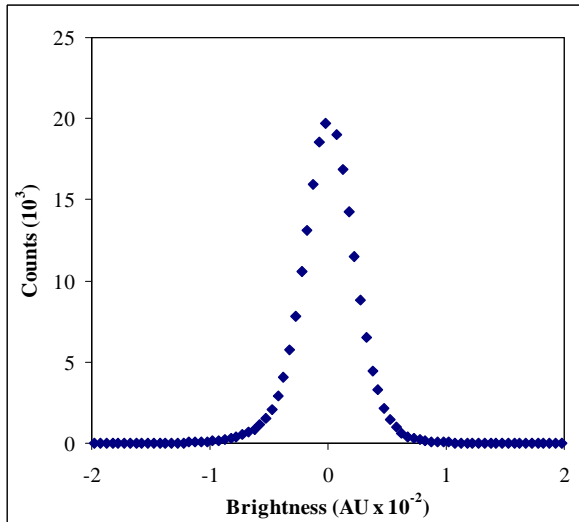
Figure 5.12: A histogram of the calibrated signal measured by all pixels above the MAS altitude in all images of the orbit shown in Figure 5.11 after the stray light has been removed. Units of brightness are those arbitrary ones used in the previous plots.

at 0, and has a standard deviation that is approximately 1% of the average stray light signal seen in Figure 5.10.

As there is a tangent height requirement for the stray light removal algorithm there is a trade-off in the benefits of the two aeronomy modes, stare and nod. The stare mode (Section 5.4.1) is the favored mode of operation for the imager. However, if the optic axis is measuring at a tangent height that precludes pixels above the MAS altitude, the stray light cannot be removed because the magnitude of the signal from outside the field of view cannot be determined. In the nod mode, if the optic axis scans down to an altitude where no pixels measure above the MAS altitude, a linear interpolation of the brightness of the stray light signal from those points in the scan before and after the altitude range where the magnitude of the stray light is unknown can be used. In this way, measurements of the lower part of the atmosphere can be made with effective stray light removal as long as the

82

nod scan does not remain at the lower altitudes for a length of time such that the magnitude of the out of field signal changes significantly. Figure 5.13 is a plot of the normalization factor for the shape of the stray light calculated for five scans of nod mode data. The magnitude of the stray light signal closely follows the tangent height of the optic axis; however, it changes in magnitude with every scan due to the brightness variations of the out of field source. There is missing data when the tangent height of the optic axis is so low that no pixels on the array measure at a tangent height above the MAS altitude.

The segments of missing data in the calculation of the normalization factor in Figure 5.13 are linearly interpolated so that the stray light removal can be made for all images in the orbit, although several different methods were investigated to determine the best fit for the missing data. One adopted method involves fitting a straight line to each side of each scan and interpolating the fits into the area of missing data below the intersection the two lines. This method, however, and others like a spline, depend on the accuracy of the satellite attitude. In some cases, the scanning attitude data for the satellite deviates so that the calculated tangent altitudes vary from those expected. In these situations, complicated fitting methods fail drastically, while a simpler solution, like the linear interpolation, provide a reliable fit. Figures 5.14 and 5.15 show a typical nod mode orbit before and after the scattered light has been removed. An interpolation of the normalization factor has been used for those tangent heights where it is not measured. The removal yields similar results to those shown for the stare mode orbit, i.e. there is no noticeable failure nor effect present for those images that used the interpolated normalization factor.
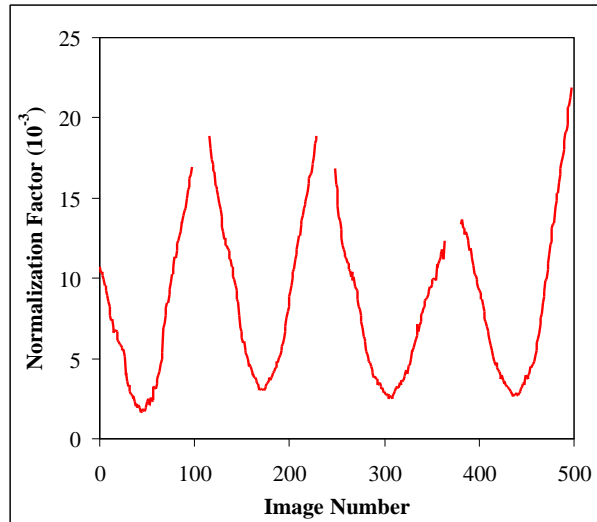
Figure 5.13: The normalization factor for the shape of the stray light signal for five scans of nod mode data. The missing data occurs when the tangent height of the optic axis is so low that no pixels measure above the MAS altitude.

5.5.2 OH Channel

The application of the stray light removal algorithm to the channel 1 OH emission and solar scattering data yields similar results to those shown for the other channels. However, as the main OH emission occurs at nighttime the stray light removal is not as critical an issue. During the daytime, channel 1 measures solar scattering, which decreases exponentially with tangent height, and a very weak daytime OH emission. Figures 5.16 and 5.17 show a typical channel 1 stare mode orbit, before and after the stray light has been removed. The stray light signal is dominant in the daytime for altitudes above 60 km. The nighttime emission, which is unaffected by stray light, is clearly evident between 75 km and 90 km altitude. After the stray light algorithm has been applied, the daytime signal decreases with increasing altitude as expected. The weak daytime OH emission that has been observed in the data product will require a special stray light removal algorithm. This procedure is currently being developed.

84
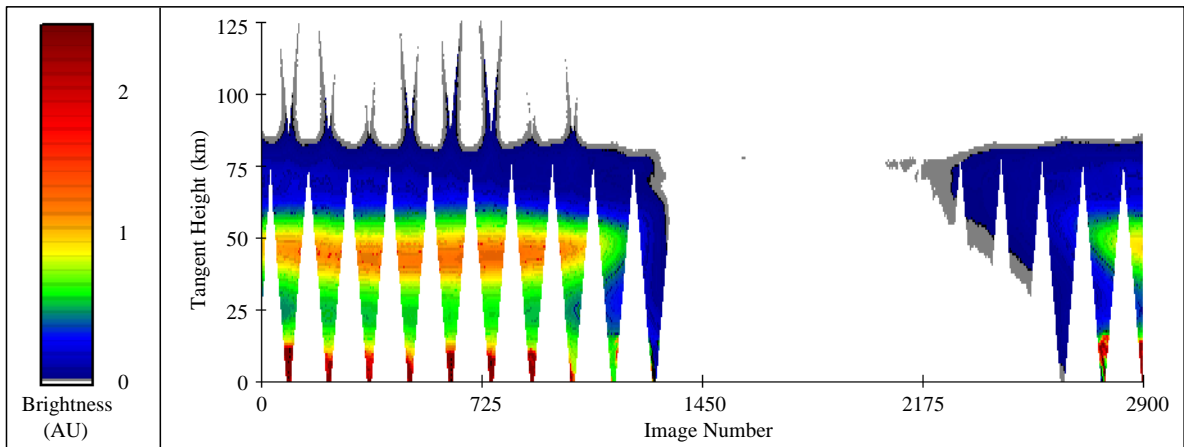
Figure 5.14: Typical $O_2(a^1\Delta_g)$ channel nod mode orbit, corrected for tangent height. Again, stray light signal is evident at higher altitudes. The triangular shaped areas of white space indicate those tangent heights that were not sampled due to the nod.
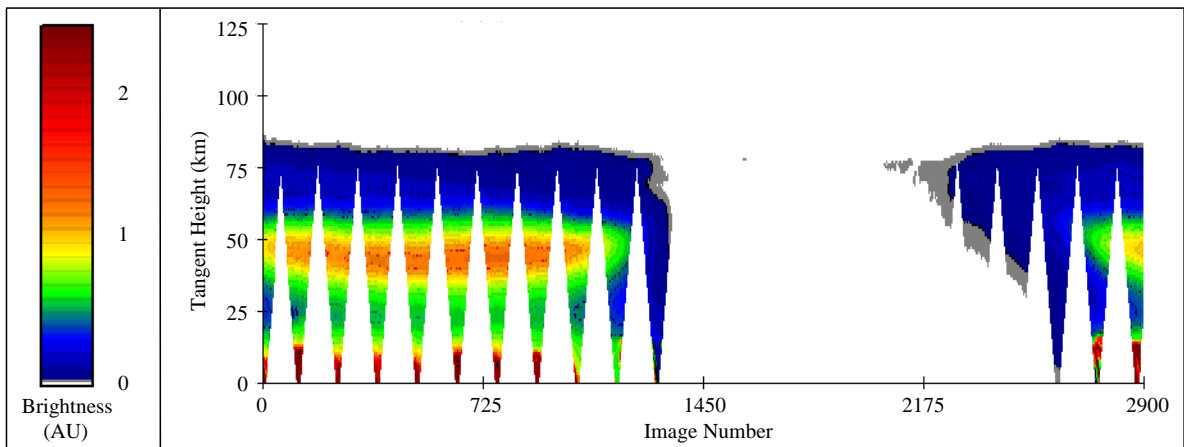
Figure 5.15: The nod mode orbit shown in Figure 5.14 after the stray light has been removed.
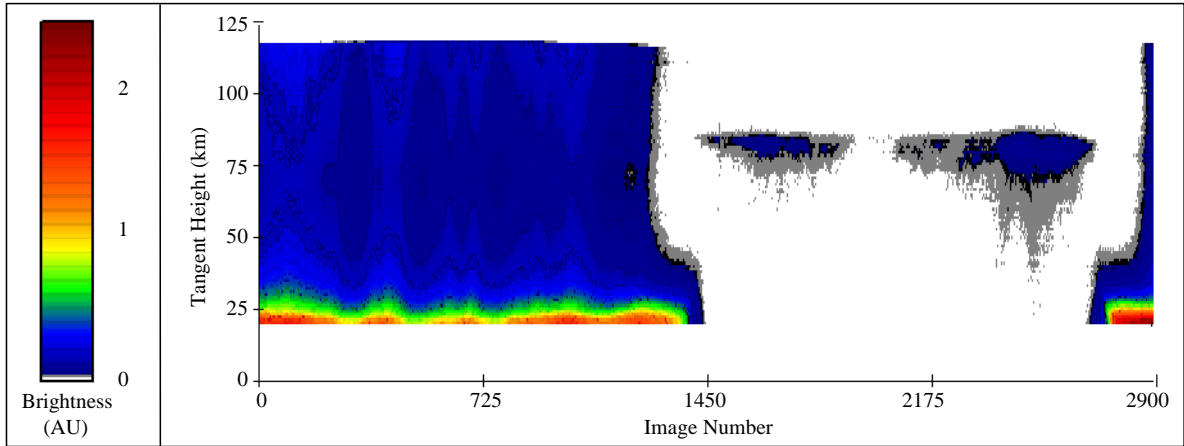
Figure 5.16: Typical OH channel stare mode orbit, corrected for tangent height. Stray light signal is dominant in the daytime for altitudes above 60 km. The night-time (images 1450-2700) emission is visible near 85 km.
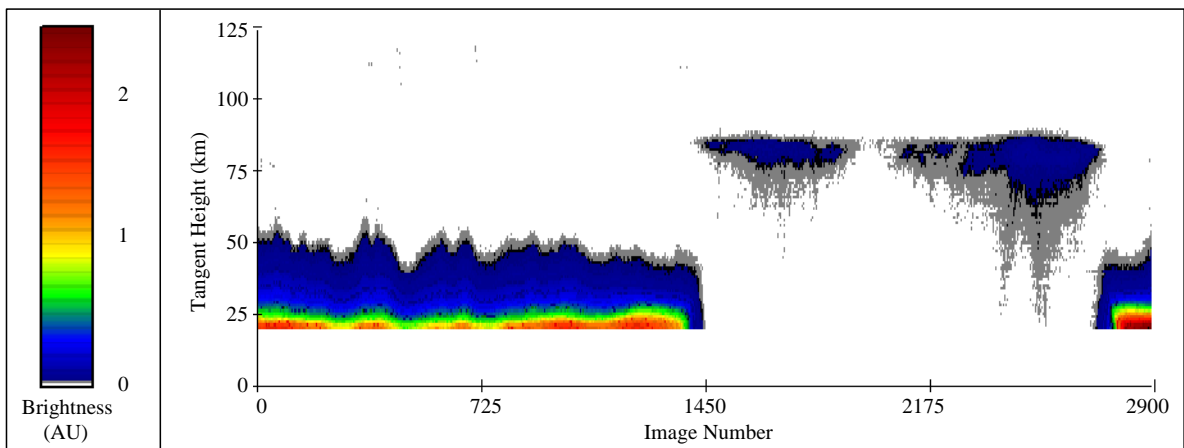
Figure 5.17: The stare mode orbit shown in Figure 5.16 after the stray light has been removed. Remaining daytime signal decreases exponentially with increasing altitude. The auto-colour scale may not be exactly the same as the one used in Figure 5.16.

Chapter 6

Absolute Calibration

6.1 Introduction

In this chapter, the preliminary absolute calibration of the imager is presented. The technique is based on pre-flight measurements of a calibrated brightness source. The calibrated in-flight measurements of scattered sunlight are then compared with the results from a simple atmospheric model that predicts the absolute brightness seen by the OSIRIS imager for the assumption of a single Rayleigh scatter approximation.

6.2 Absolute Calibration: Definition and Units

The absolute calibration of the imager involves the conversion of the digital number reported by the read-out electronics of the A/D converter, after all instrument dependant effects have been removed, to a physical brightness with appropriate units. The brightness of a source, B_s, is typically reported in terms of the number of photons, in a given wavelength range, emitted per second on from unit area within unit solid angle, or

$$[B_{\mathrm{s}}] = \frac{\text{photons}}{\text{s cm}^2 \text{ nm sterad}}.$$

(6.1)

The brightness along a line of sight measured by the imager, B_o, is an integral of the wavelength dependent source brightness across the wavelength range of the filter as discussed in Chapter 4.

$$B_o = \int B_s(\lambda) f(\lambda) \tau(\lambda) \mathrm{d}\lambda. \tag{6.2}$$

Thus the units of this brightness are

$$[B_o] = \frac{\text{photons}}{\text{s cm}^2 \text{ sterad}}. \tag{6.3}$$

6.3 Pre-Flight Data

6.3.1 Calibrated Source Technique

If a source with a known brightness at all wavelengths is available, then absolute calibration of the imager is straight forward. Then if the arbitrary units of observation, in this case, DN, scale linearly with incident brightness, a calibration constant, α, which relates the physical units of brightness to the observation units, can be determined with a single measurement of the source. If the observations, O_s, have been relatively calibrated, i.e. on a pixel to pixel basis, then the measured brightness, B_o is

$$B_o = \alpha \, O_s. \tag{6.4}$$

Hence a single measurement of a calibrated source (see Equation 6.2), allows the quantity α to be determined as

$$\alpha = \frac{\int B_s(\lambda) f(\lambda) \tau(\lambda) \mathrm{d}\lambda}{O_s}. \tag{6.5}$$

6.3.2 Calgary Data Sessions

In the Calgary pre-flight calibration, several images were taken of a calibrated 6 W low brightness source. The brightness of this lamp had been measured at NIST

at discrete points wavelengths in terms of $\frac{W}{cm^2\ \mu m\ sterad}$; the filter shape in the instrument was measured at a number of wavelengths. At each measured wavelength in the filter shape the lamp brightness is determined from a linear interpolation between adjacent known values. The product of the filter shape and the lamp brightness is then determined on a point by point basis, in terms of $\frac{photons}{s\ cm^2\ ster}$ using the photon-energy relationship,

$$E = \frac{h\ c}{\lambda}\ \frac{J}{photon}. \tag{6.6}$$

The filter shape – lamp brightness product is then integrated numerically to determine B_o. An average of several observations of the source with the imager, after dark calibration and flat field have been applied, are used (Equation 6.5) to determine the absolute calibration constant, α.

6.4   In-Flight Data

6.4.1   Single Rayleigh Scatter Model

A simple "reality check" of the measured absolute calibration has been made with a standard Rayleigh scattering model for the atmospheric brightness. The model considers only single Rayleigh scattered light for an atmospheric density profile that is assumed to be representative of the atmospheric for any location. The limb look vector and the satellite position, which together determine the path length though the atmosphere, and the solar vector are the only variable parameters in the model. No corrections are included for multiple scattering, albedo, or molecular emission and absorption. For comparison with the imager measurements, the differential brightness is modelled using the transmission of a standardized zero air mass solar spectrum at several wavelengths across the filter shape. The product of the modelled brightness and the filter transmission is then integrated with respect to wavelength to yield results that can be compared with the calibrated imager observations.

6.4.2   OH Channel

The OH channel, which has a 40 nm wide filter centered at 1.53 μm, makes measurements that are dominated by scattered sunlight in the daytime and by the OH Meinel band molecular emissions at night. It should be noted that this channel does not suffer the problems with the relative gain calibration that are evident in the singlet delta channels. The flat field parameters that were measured in Calgary are directly applied to the in-flight data processing. There is no reason to believe that the absolute gain has changed since the launch so that the absolute calibration constant as determined from the pre-flight calibration (Section 6.3.1) is directly applied to the in-flight data.

Figure 6.1 is a plot of the measured and modelled absolute brightness for channel 1. These data correspond to a constant tangent height, 30 km, and are plotted as a function of solar zenith angle. Sunset at 30 km altitude corresponds to a solar zenith angle of approximately 95.5°. As only single Rayleigh scattering is considered, the modelled brightness is essentially a constant value for all solar zenith angles less than 95.5°. Once the sun has gone below the horizon, the brightness decreases exponentially as the path length through the sunlit atmosphere decreases. The measured brightness compares very well with the modelled values for solar zenith angles beyond sunset (greater than 95.5°). For lower solar zenith angles, those less than 95.5°, where the atmosphere below 30 km is illuminated, the measured brightness is systematically higher than the modelled result. This is attributed to multiple scattering from the more dense atmosphere below. The continued increase and further variation in the measured signal for smaller solar zenith angles, i.e. less than 90° where the ground below the tangent point is illuminated, can be attributed to the albedo of the earth as well as multiple scattering. The reflection of the scattering sunlight from the surface of the earth varies with location along the satellite track and so also varies with solar zenith angle.

For solar zenith angles greater than 95.5°, the effects of multiple scattering and albedo, which are not considered in the model, are minimized. In this region, the

90
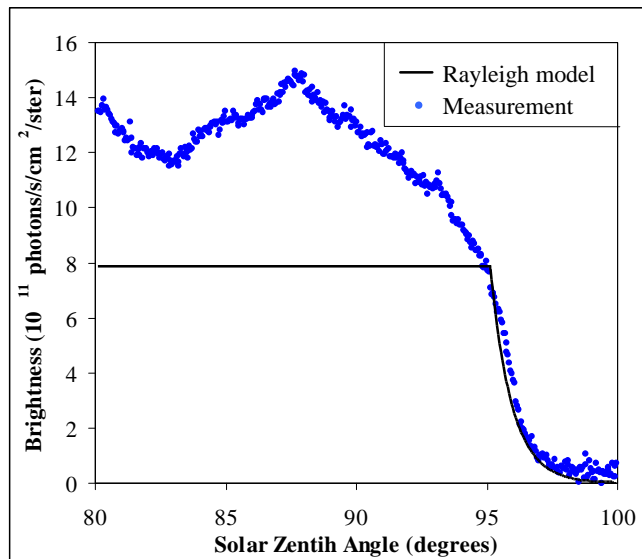
Figure 6.1: Modelled and measured brightness as a function of solar zenith angle at a constant tangent height of 30 km.

modelled result is within 10% of the measurement. Similar results are found for measurements from several different orbits and over a height range that provides sufficient signal levels without dropping so low that it is dominated by multiple scattering terms. Overall, this comparison provides a first order verification of the absolute calibration of channel 1.

6.4.3 $O_2(a^1\Delta_g)$ Channels

The other two channels of the imager suffer from the odd/even effect of relative gain calibration that was discussed in detail in Chapter 4. Because of this effect, the flat field parameters calculated from the pre-flight Calgary calibration sessions were deemed invalid. It follows that if the these gain parameters cannot be used, then the measurements of the absolute calibration source must also be questioned.

In addition, because the $O_2(a^1\Delta_g)$ airglow emission is extremely bright, these channels cannot be compared to the single Rayleigh scatter model in the same fash-

ion as channel 1. The brightness of the airglow is comparable with the brightness of the Rayleigh scattering below 30 km. Without a complicated tomographic retrieval, which can calculate actual volume emission rates from the limb line of sight observations, the actual magnitude of the scattered sunlight is difficult to determine.

As a current best effort, the odd pixels in these two channels are assumed to have remained constant while the even pixels are assumed to have suffered a relative change in gain. The reason the odd pixels were chosen is because, as shown in Figure 4.9, the odd pixels seem to have remained constant in their response relative to each other, whereas the even pixels have changed their relative response to a Lambertian source. This being the case, after the in-flight flat field parameters, which correct the odd/even effect, are applied, the absolute calibration constant determined in Calgary for the odd pixels is applied to the entire detector.

The odd/even effect causes variation in gain on the order of 20 to 30%. This could translate into a systematic error in the absolute calibration of at least this amount. Once the measurements are further processed with the tomographic inversions and the first ozone profiles calculated, a validation of the absolute calibration can be made by comparison with other validated satellite ozone profiles from the OSIRIS spectrograph, the Odin SMR, or instruments on other satellites.

Chapter 7

Summary and Conclusions

7.1 Summary of the Present Work

In the present work, the identification of instrument dependent effects that modify the measurement of the airglow brightness by OSIRIS imager has been presented. An attempt has been made to understand fully the causes of each effect so that they can be reliably characterized and removed.

An investigation of the dark current has shown that the main production mechanisms depend on the small bias of the photodiode amplifier configuration. Under reverse bias the dark current is dominated by thermally generated carriers, and, under forward bias by the recombination current. A technique for the characterization and removal of the dark current in a linear array has been presented that is capable of removing dark current, even when there is a randomly varying electronic image offset. The technique relies on the difference between a signal pixel and a pixel that is under the detector mask that is therefore always measuring a dark signal. The effectiveness of the technique is limited by the shot noise in the detectors that necessarily increases with temperature and exposure time. The dark current characteristics of each pixel change slowly over the period of months. For the satellite mission, new parameters are calculated every month based on in-flight dark images.

The relative calibration of pixels in the array has considered two main effects: the relative gain and the look direction. Considerable effort has been put into an attempt to understand an apparent change in the gain of the odd and even sides of imager channels 2 and 3 between pre-flight calibration and in-flight data. A method that uses in-flight data to approximate a constant brightness source has been developed to allow re-calculation of the flat field parameters. Application of these parameters produces consistently smooth height profiles; however, it has been necessary to assume an average filter shape for all pixels on a channel. It is shown that this assumption may lead to systematic errors of a few percent in the integrated brightness of the airglow due to changes in the band emission with height and atmospheric temperature. The relative look direction has been investigated through independent in-flight experiments (Degenstein, 2002; Lloyd, 2002). The results of these experiments agree within a few percent and it has been shown that tangent height brightness measurements of the steady-state midday emission peak with different pixels produce no obvious differences that can be correlated with the relative line of sight of each pixel.

There is significant out-of-field, or stray, light observed in the flight data. A technique to characterize and extrapolate the shape of the stray light signal on the detector has been developed by normalizing the stray light signal with the magnitude of the signal above the MAS (Minimum Atmospheric Signal) altitude. The error in the technique, as indicated by tangent heights that contain no atmospheric scattering or emission, is random and relatively small compared with the magnitude of the stray light signal.

The absolute calibration of channel 1 has been made directly with pre-flight measurements of a calibrated brightness source. Comparison with a single Rayleigh scatter model produces similar results in those regions where the effects of multiple scatter and albedo terms are minimized. Absolute calibration for channels 2 and 3 is complicated by the observed changes in the relative gain of the odd and even pixels. However, with appropriate assumptions, the pre-flight calibration can be used. In

these cases a comparison with the scattered sunlight model cannot be made because of the atmospheric absorption and the airglow emission in these channels. It is suggested that the absolute calibration must await a comparison of derived ozone profiles with those from other instruments.

Software has been developed that can apply these corrections in an automated data processing chain. Figure 7.1 is a flow chart of the software operation. The main stages of the processing are shown as coloured circles in the central rectangle. This flow chart was developed in the initial stages of the processing work. It has been presented several times at meetings of the Canadian OSIRIS science team. The colour of the processing stage signifies the present degree of confidence in the correctness and completion of each stage. At the beginning of this work all four circles were red. This signified an inability to process any stage. Currently, as shown in the chart, the first three stages, dark current, stray light, and flat field are shown in green and are processed in an automated fashion with a high degree of confidence. The only remaining stage, the absolute calibration, is shown in yellow. This means that processing is ongoing, although issues remain that still need to be addressed.

The dramatic effects of the application of the processing stages are best shown by the two images in Figure 7.2. Each of these images is a plot of the same full orbit of 1.53 μm data. The first plot is uncalibrated data exactly as it comes down from the satellite in terms of image number and pixel number. Sunrise occurs near the beginning of the orbit and sunset at approximately image 1200. The second plot shows the same data after the full calibration has been applied; in this case it is plotted as a function of tangent height and image number. The nighttime OH emission, completely undetectable in the raw data, is readily evident after calibration. Also, in the middle of the daytime there is a region of enhanced scattering near 80 km that is believed to be a Polar Mesospheric Cloud, or PMC. Again, this feature cannot be discerned in the raw data product.
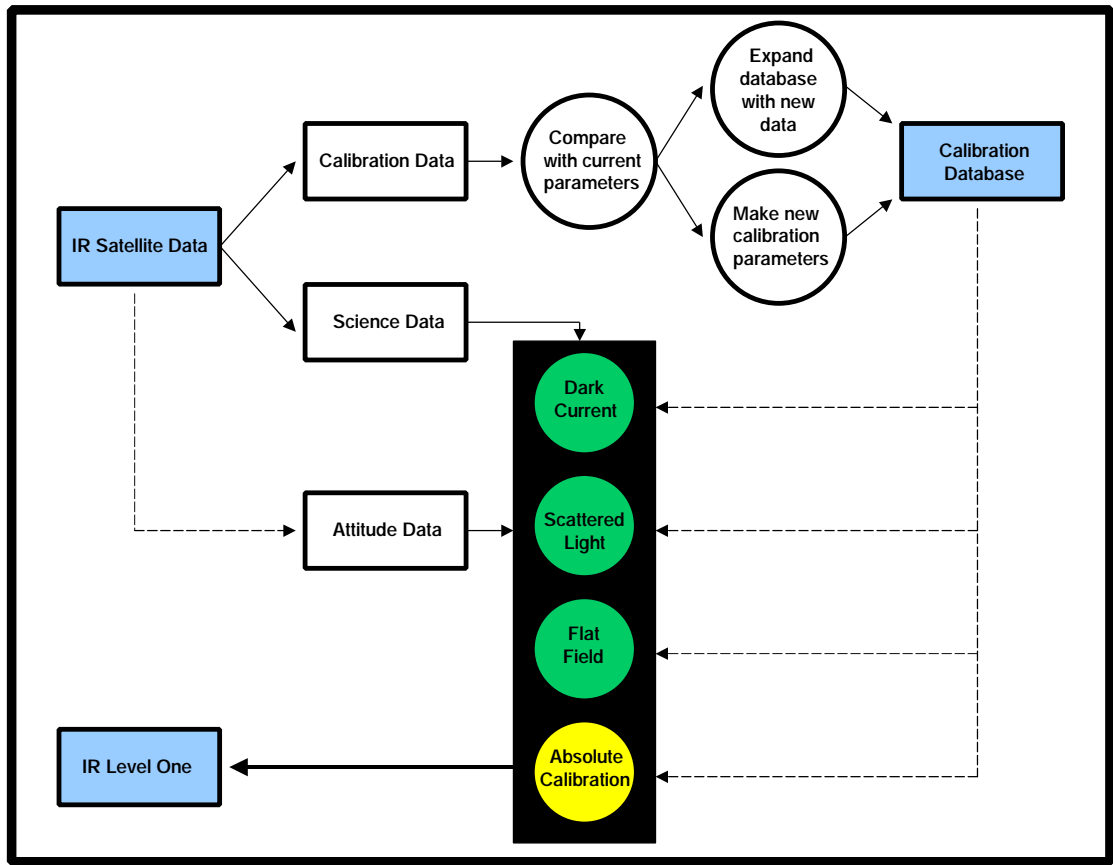
Figure 7.1: Current state of the automated calibration processing chain for the OSIRIS imager.

Figure 7.2: One orbit of 1.53 μm nod mode data shown before and after the full calibration. The nighttime OH emission and a region of enhanced scattering in the daytime (believed to be a Polar Me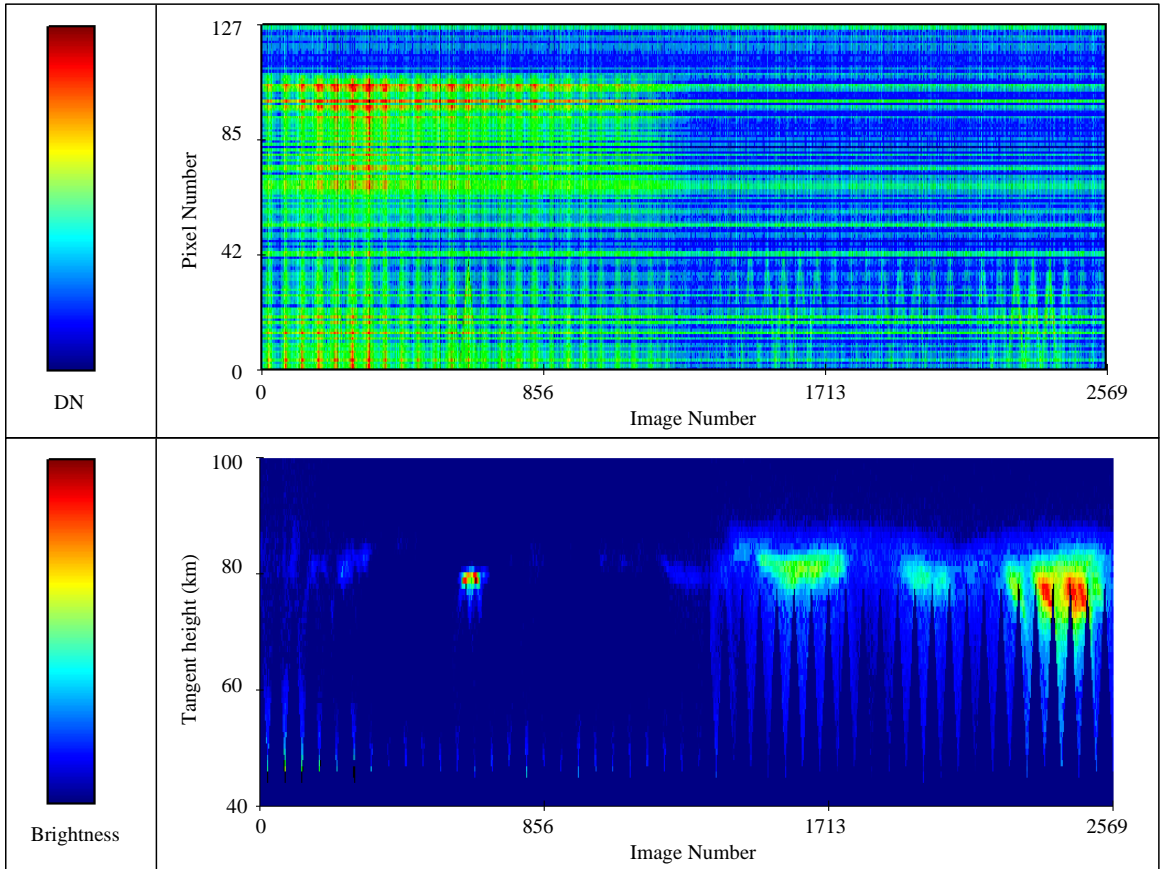sospheric Cloud) that cannot be discerned in the raw data are impressive in the fully calibrated orbit. The nod structure visible in the calibrated product is due to missing data.

97

7.2 Recommendations for Future Work

The main work yet to be done with imager flight data is a thorough investigation of the absolute calibration, especially for the singlet delta channels. However, this work must be delayed until the inversions of the observations are completed with confidence. At that point, the brightness of the altitude profiles can be compared with previous measurements and ozone profiles can be derived and compared with those from other instruments. Without a full knowledge of the apparent changes in the relative gain of the pixels an independent absolute calibration of these channels will be very difficult.

References

Barth, C.A., D.W. Rusch, R.J. Thomas, G.H. Mount, G.J. Rottman, G.E. Thomas, R.W. Sanders, and G.M. Lawrence: "Solar Mesospheric Explorer: Scientific Objectives and Results", *Geophys. Res. Letters*, **10**, 237, 1983.

Bantle, M., E.J. Llewellyn, and B.H. Solheim: "Measurement of $O_2(a^1\Delta_g)$ Emission in a Total Solar Eclipse", *J. Atmos. Terr. Phys.*, **46**, 265, 1983.

Caldwell, M.E., and P.F. Gray: "Application of a Generalized Diffraction Analysis to the Design of Nonstandard Lyot-stop Systems for Earth Limb Viewing Radiometers", *Opt. Eng.*, **36**, 2793, 1997.

Degenstein, D.A.: Private correspondence regarding in-flight relative look direction experiment, 2002.

Degenstein, D.A., E.J. Llewellyn, and N.D. Lloyd: "Volume Emission Rate Tomography from a Satellite Platform", *Applied Optics*, **42**, 1441, 2003.

Evans, W.F.J., E.J. Llewellyn, and A. Vallance Jones: "Balloon-borne Observations of the Brightness Variations in the (0,0) Band of the $(^1\Delta_g - ^3\Sigma_g)$ System of Oxygen in the Day and Twilight Airglow", *Nature*, **213**, 352, 1967.

Evans, W.F.J., D.M. Hunten, E.J. Llewellyn, and A. Vallance Jones: "Altitude Profile of the Infrared Atmospheric System of Oxygen in the Dayglow", *J. Geophys. Res.*, **73**, 2885, 1968.

Evans, W.F.J., and E.J. Llewellyn: "Atomic Hydrogen Concentrations in the Mesosphere and the Hydroxyl Emissions", *J. Geophys. Res.*, **78**, 323, 1973.

Gattinger, R.L., and A. Vallance Jones: "The $^1\Delta_g - ^3\Sigma_g$ Bands in the Twilight and Day Airglow", *Planet. Space Sci.*, **14**, 1, 1966.

Haslett, J.C., and L.R. Megill: "Rocket Measurements of $O_2(^1\Delta_g)$", *Can. J. Phys.*, **47**, 2351, 1969.

Herzberg, G.: "Photography of the Infra-Red Solar Spectrum to Wavelength 12,900 Å", *Nature*, **133**, 759, 1934.

Ivanov, E.: "Computer Modelling of the OSIRIS Infrared Imager", M.Sc. Thesis, University of Saskatchewan, 2000.

Kasap, S.O.: Optoelectronics and Photonics. Prentice Hall, 2001.

Llewellyn, E.J., B.H. Long, and B.H. Solheim: "The Quenching of OH* in the Atmoshere", *Planet. Space Sci.*, **26**, 525, 1978.

Llewellyn, E.J., and B.H. Solheim: "The Excitation of the Infrared Atmospheric Oxygen Bands in the Nightglow", *Planet. Space Sci.*, **26**, 533, 1978.

Lloyd, N. D.: "OSIRIS Beam Alignment Results from Toulouse, September 2000", *Internal document*, 2000.

Lloyd, N. D.: "OSIRIS Jupiter Alignment", *Internal document*, 2002.

López-González, M.J., J.J. López-Moreno, M.A. López-Valverde, and R. Rodrigo: "Behavior of the O_2 Infrared Atmospheric (0-0) Band in the Middle Atmosphere During Evening Twilight and at Night", *Planet. Space Sci.*, **37**, 61, 1989.

Marsh, D., A. Smith, G. Brasseur, M. Kaufmann, and K. Grossmann: "The Existence of a Tertiary Ozone Maximum in the High-Latitude Middle Mesophere", *Geophys. Res. Letters*, **28**, 4531, 2001.

Mlynczak, M.G., S. Solomon, and D.S. Zaras: "An Updated Model for $O_2(a^1\Delta_g)$ Concentrations in the Mesosphere and Lower Thermosphere and Implications for Remote Sensing of Ozone at 1.27 μm", *J. Geophys. Res.*, **98**, 18639, 1993.

Mlynczak, M.G., and D.S. Olander: "On the Utility of the Molecular Oxygen Dayglow Emissions as Proxies for Middle Atmospheric Ozone", *Geophys. Res. Letters*, **22**, 1377, 1995.

Murtagh, D., U. Frisk, F. Merino, M. Ridal, A. Jonsson, J. Stegman, G. Witt, P. Eriksson, C. Jimenez, G. Mègie, J. de la Nöe, P. Ricaud, P. Baron, J. Pardo, A. Hauchcorne, E. J. Llewellyn, D. Degenstein, R. Gattinger, N. Lloyd, W. Evans, I. McDade, C. Haley, C. Sioris, C. von Savigny, B. Solheim, J. McConnell, K. Strong, E. Richardson, G. Leppelmeier, E. Kyrola, H. Auvinen, and L. Oikarinen: "An Overview of the Odin Atmospheric Mission", *Can. J. Phys.*, **80**, 309, 2002.

Noxon, J.F., and A. Vallance Jones: "Observation of (0,0) Band of the $(^1\Delta_g - ^3\Sigma_g)$ System of Oxygen in the Day and Twilight Airglow", *Nature*, **196**, 157, 1962.

Sica, R. J.: "Inferring Middle-Atmospheric Ozone Height Profiles From Ground Based Measurements of Molecular Oxygen Emission Rates", *Can. J. Phys.*, **69**, 1069, 1991.

Thomas, R.J., C.A. Barth, G.J. Rottman, D.W. Rusch, G.H. Mount, G.M. Lawrence, R.W. Sanders, G.E. Thomas, and L.E. Clemens: "Ozone Density Distribution in the Mesosphere Measured by the SME Limb Scanning Near Infrared Spectrometer", *Geophys. Res. Letters*, **10**, 245, 1983.

Vallance Jones, A., and R.L. Gattinger: "The Seasonal Variation and Excitation Mechanism of the 1.58 μ $^1\Delta_g - ^3\Sigma_g$ Twilight Airglow Band", *Planet. Space Sci.*, **11**, 961, 1963.

Vallance Jones, A., and A.W. Harrison: "$^1\Delta_g - ^3\Sigma_g$ O_2 Infrared Emission Band in the Twilight Airglow Spectrum", *J. Atmos. Terr. Phys.*, **13**, 45, 1958.

Wood, H.C.: "The Measurement and Interpretation of $O_2(a^1\Delta_g)$ Concentrations in the Atmosphere", Ph.D. Thesis, University of Saskatchewan, 1972.